AGU PUBLICATIONS

Tectonics

RESEARCH ARTICLE
10.1002/2016TC004177

Key Points:
- Counterclockwise *P-T* paths involving near-isotherm compression record crustal thickening from arc to forearc
- Circa 830–800 Ma metamorphic zircon ages are linked to the initial cooling and exhumation stage
- The first mid-Neoproterozoic *P-T-t* path links the Tarim Craton to the circum-Rodinia subduction system

Supporting Information:
- Supporting Information S1
- Table S1
- Table S2
- Table S3
- Table S4
- Table S5

Correspondence to:
R. Ge, W. Zhu, and S. Wilde,
gerongfeng@nju.edu.cn;
zwb@nju.edu.cn;
S.Wilde@curtin.edu.au

Citation:
Ge, R., W. Zhu, and S. A. Wilde (2016), Mid-Neoproterozoic (ca. 830–800 Ma) metamorphic *P-T* paths link Tarim to the circum-Rodinia subduction-accretion system, *Tectonics*, *35*, 1465–1488, doi:10.1002/2016TC004177.

Received 12 MAR 2016
Accepted 27 MAY 2016
Accepted article online 4 JUN 2016
Published online 22 JUN 2016

Mid-Neoproterozoic (ca. 830–800 Ma) metamorphic *P-T* paths link Tarim to the circum-Rodinia subduction-accretion system

Rongfeng Ge[1,2], Wenbin Zhu[1], and Simon A. Wilde[2]

[1]State Key Laboratory for Mineral Deposits Research, School of Earth Sciences and Engineering, Nanjing University, Nanjing, China, [2]Department of Applied Geology, Curtin University, Perth, Western Australia, Australia

Abstract Long-lived exterior accretionary orogeny shapes tectonothermal evolution of the peripheral building blocks of supercontinents and leads to considerable crustal growth. However, such accretionary orogeny has only been locally recognized for the Rodinia supercontinent. Here a suite of newly discovered mid-Neoproterozoic high-grade metamorphic rocks in the northern Tarim Craton, NW China, are used to test the exterior accretion hypothesis for Rodinia. These rocks occur as dark-colored mafic and calc-silicate boudins in impure marbles and mica schists. Geochemical data suggest a protolith of arc-related basalts metasomatized by Ca-rich fluids. Mineral assemblages, phase diagram modeling, and mineral compositions for a garnet pyroxenite and a garnet clinopyroxene gneiss reveal upper amphibolite to high-pressure granulite facies peak metamorphism (660–700°C, 11–12 kbar) following a counterclockwise *P-T* path, which is characterized by prograde burial and heating, followed by near-isothermal burial and retrograde exhumation and cooling. This *P-T* path is interpreted to have recorded crustal thickening of an earlier magmatic arc transformed to a fore arc by subduction erosion and subsequent burial along bent isotherms near the subduction channel. All studied samples record ca. 830–800 Ma metamorphic zircon U-Pb ages, which probably date the early exhumation and cooling according to Ti-in-zircon temperatures, zircon rare earth element patterns, and Hf isotopes. This is the first mid-Neoproterozoic *P-T-t* path in Tarim, and it provides metamorphic evidence for a mid-Neoproterozoic advancing-type accretionary orogeny, which is coeval with the initial breakup events of Rodinia and thus links Tarim to the circum-Rodinia accretion system, supporting the peripheral subduction model.

1. Introduction

Supercontinents assemble and break apart, respectively, by global-scale collisional orogeny and continental rifting. In contrast, exterior oceanic subduction and accretionary orogeny commonly occur at the periphery of supercontinents after final assembly in order to balance ongoing seafloor spreading in the circumsupercontinent ocean [e.g., *Murphy and Nance*, 1991; *Cawood and Buchan*, 2007]. Such peripheral subduction and accretion may last until the final breakup of the supercontinent and may lead to considerable continental growth through juvenile arc magmatism and tectonic accretion. These processes are likely to have major impacts on continental blocks located at the margin of the supercontinent, as have been documented for Pangea, Gondwana, and Nuna (aka Columbia) [e.g., *Zhao et al.*, 2004; *Cawood*, 2005; *Cawood and Buchan*, 2007]. Such long-lived peripheral subduction-accretion is also important to understanding the geodynamic evolution of supercontinents. *Li and Zhong* [2009] proposed that it was the circum-supercontinent subduction that triggers the formation of antipodal superplumes that eventually lead to the breakup of supercontinents.

The Rodinia supercontinent is generally accepted to have assembled and broken apart through ca. 1300–900 Ma global-scale collisional orogenesis and subsequent ca. 830–600 Ma continental rifting, respectively [e.g., *Hoffman*, 1991; *Li et al.*, 2008; *Evans*, 2009]. Since the seminal studies in the 1990s [e.g., *Dalziel*, 1991; *Hoffman*, 1991; *Moores*, 1991], much attention has been paid to interior collisional and rifting processes to resolve the evolution and configuration of the supercontinent [e.g., *Li et al.*, 2008; *Evans*, 2013, and references therein]. Oceanic subduction and accretion at the periphery of Rodinia, although briefly outlined in several recent Rodinia reconstructions [e.g., *Li et al.*, 2008; *Cawood et al.*, 2013], has only been locally documented in the geological record (e.g., the Valhalla Orogen) [*Cawood et al.*, 2010], and its influence on the tectonothermal evolution of the peripheral blocks has not been well appreciated.

The Tarim Craton in northwestern China has been considered as a building block of the Rodinia supercontinent [e.g., *Hoffman*, 1991; *Li et al*., 2008; *Evans*, 2009]. It represents an ideal place to test the periphery subduction-accretion hypothesis for Rodinia, because recent comparative studies of Neoproterozoic tillite-bearing strata [e.g., *Li et al*., 1996; *Xu et al*., 2009; *He et al*., 2014a], magmatic sequences [e.g., *Lu et al*., 2008; *Shu et al*., 2011; *Zhang et al*., 2012a], and paleomagnetic poles [e.g., *Chen et al*., 2004; *Wen et al*., 2013; *Zhao et al*., 2014] have shown that Tarim was likely situated at the northwestern margin of Rodinia close to Australia and South China, although specific relative positions are still debated. *Ge et al*. [2014a] proposed a long-lived Neoproterozoic (950–600 Ma) subduction-accretion model for the northern Tarim Craton and correlated it with the global-scale circum-Rodinia subduction-accretion system. This model challenges the prevailing view that considered that the Mesoproterozoic to early Neoproterozoic (ca. 1050–900 Ma) and middle to late Neoproterozoic (ca. 830–600 Ma) tectonothermal events in Tarim were related to the assembly and breakup of Rodinia, respectively [e.g., *Lu et al*., 2008; *Shu et al*., 2011; *Long et al*., 2011; *Zhang et al*., 2012a]. The new model is mainly based on a different interpretation of geochemical data for the ca. 830–615 Ma magmatic rocks, and metamorphic and structural evidence for a Neoproterozoic accretionary orogeny is still lacking. Recently, *He et al*. [2012] reported a suite of granulite facies metamorphic rocks in the northernmost Tarim Craton with metamorphic zircon U-Pb ages of ca. 820–790 Ma, coeval with the early breakup events of Rodinia. However, the tectonic setting of this mid-Neoproterozoic metamorphism remains ambiguous due to lack of a reliable *P-T-t* path. Clearly, confirming the regional extent and tectonic setting of this high-grade metamorphism is critical to understanding the Neoproterozoic tectonic evolution of the Tarim Craton and to evaluating its relevance to the peripheral subduction-accretion process of Rodinia.

Here we present a metamorphic study of a suite of newly discovered mid-Neoproterozoic high-grade mafic and calc-silicate rocks in the Korla area of the northern Tarim Craton. Detailed field, geochemical, petrographic, phase diagram modeling and in situ zircon U-Pb-Hf isotopic and trace element data are used (1) to determine the protolith, metamorphic *P-T* conditions, and zircon U-Pb ages of these rocks; (2) to link the metamorphic zircon ages to metamorphic evolution and establish the *P-T-t* path; and (3) to evaluate the tectonic setting of metamorphism in the Tarim Craton and its relevance to the circum-Rodinia subduction-accretion system.

2. Geological Setting and Samples

The Tarim Craton is a ~600,000 km^2 eye-shaped continental block in NW China. It is surrounded by the Central Asian Orogenic Belt (CAOB) to the north and the Tibetan Plateau to the south (Figure 1a). It is largely covered by late Neoproterozoic to Cenozoic strata in the center, and earlier Precambrian rocks are only exposed in the marginal blocks, namely, the Kuruktag (i.e., Quruqtagh or Kuluketage), Aksu, and Dunhuang blocks in the north and the Tiekelike and Altyn Tagh blocks in the south (Figure 1b). Geochronological data show that the oldest rocks are Neoarchean (age peaks at 2.55 and 2.71 Ga) TTG (tonalite - trondhjemite - granodiorite) gneisses and metavolcanic rocks [e.g., *Long et al*., 2010, 2014; *Zong et al*., 2013; *Ge et al*., 2014b; *Zhang et al*., 2013, 2014] and rare 2.8–3.1 Ga gneisses [*Gehrels et al*., 2003; *Lu et al*., 2008; *Zhao et al*., 2015], although the presence of ca. 3.6 Ga inherited zircons [*Lu et al*., 2008] and ca. 3.5 Ga detrital zircons with 3.9–3.7 Ga Hf model ages [*Ge et al*., 2014c] implies the existence of Paleoarchean to Eoarchean crustal components. A significant late Paleoproterozoic (1.8–2.1 Ga) tectonothermal event has been documented recently, and this has been attributed to subduction and collisional events related to the docking of Tarim to the Nuna supercontinent [e.g., *Dong et al*., 2011; *Zhang et al*., 2012b, 2012c; *He et al*., 2013; *Ge et al*., 2013a, 2013b, 2015].

An important Neoproterozoic tectonothermal event, named the Tarimian Orogeny, occurred in the Tarim Craton, resulting in extensive magmatism and regional metamorphism and deformation [e.g., *Lu*, 1992; *Gao et al*., 1993; *XBGMR*, 1993]. Based on a few imprecise $^{40}Ar/^{39}Ar$, whole-rock Sm-Nd and zircon U-Pb ages, some researchers assigned a Grenvillian age to the Tarimian Orogeny and speculated that it was a response to global-scale collisional events related to Rodinia assembly [*Lu et al*., 2008; *Zhang et al*., 2003, 2012a, 2012b; *Shu et al*., 2011; *Kröner et al*., 2013a]. Recent geochronological studies have demonstrated abundant ca. 0.95–0.90 Ga granitoids in the Yili-Central Tianshan blocks [e.g., *Huang et al*., 2014; *Gao et al*., 2015; *Yuan et al*., 2015] and the Altyn Tagh-Qilian-Quanji blocks [e.g., *Song et al*., 2012; *Yu et al*., 2013; *Wang et al*., 2013] to the north and southeast of the Tarim Craton, respectively. These magmatic events are much younger

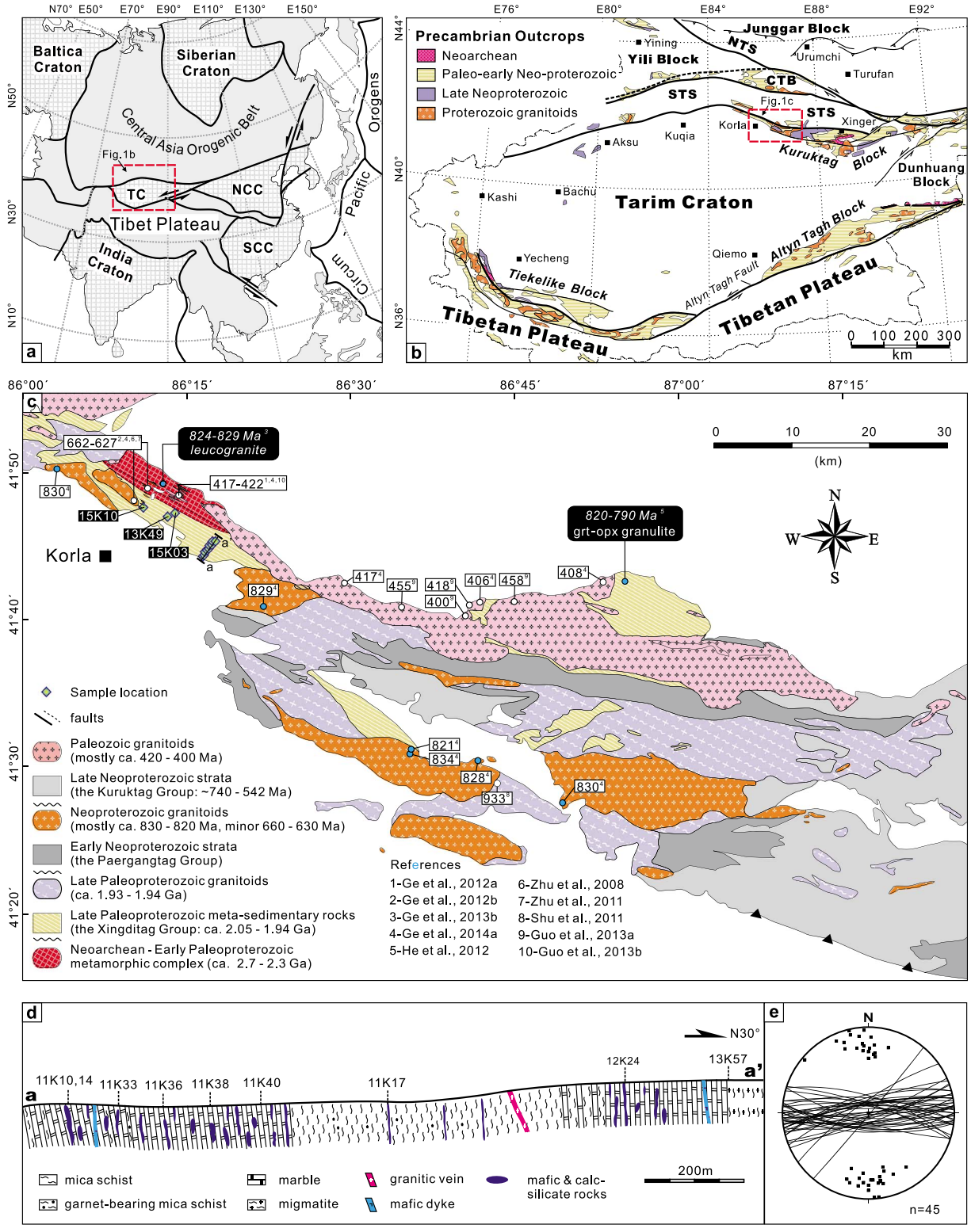

Figure 1. (a) Simplified tectonic map of Eurasia showing the major tectonic units and the location of the Tarim Craton (TC); NCC: North China Craton; SCC: South China Craton. (b) Simplified geological map of Precambrian rocks in the Tarim Craton showing the location of the study area (modified after *XBGMR* [1993]). STS: Southern Tianshan; NTS: Northern Tianshan; CTB: Central Tianshan Block. (c) Geological map of the western Kuruktag Block (modified after *XBGMR* [1959]). The locations of the studied samples are shown, and the locations of ca. 830–800 Ma leucogranites [*Ge et al*., 2013b] and ca. 820–790 Ma granulites [*He et al*., 2012] are also indicated. (d) A measured cross section (a–a', location shown in Figure 1c) showing the occurrence of the studied metamafic and calc-silicate rocks. (e) Stereographic projection (lower hemisphere) of the main foliation on the measured cross section.

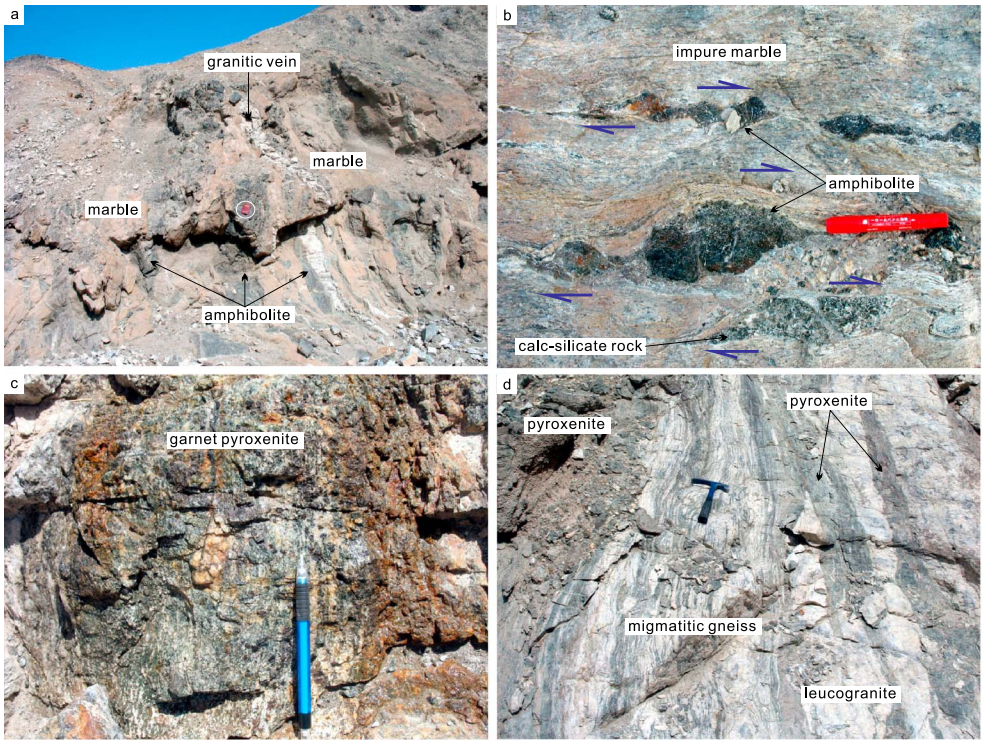

Figure 2. Field photographs showing the main lithologies and their field relations in the Korla area. (a) amphibolite boudins in reddish coarse-grained marble cut by a granitic vein (field notebook (circled) for scale); (b) amphibolite and calc-silicate boudins in impure marble showing dextral horizontal shearing; (c) garnet pyroxenite boudin (sample 11K17); and (d) migmatitic gneiss associated with melanocratic pyroxenite and leucogranitic veins.

than typical Grenvillian orogenic events (1.3–1.0 Ga) [e.g., *Rivers*, 1997]. In contrast, extensive and diverse magmatic rocks were emplaced during ca. 830–615 Ma in the Tarim Craton [*Zhu et al*., 2011a; *Zhang et al*., 2012a; *Ge et al*., 2012a, and references therein]. These middle to late Neoproterozoic magmatic rocks are commonly attributed to rifting events related to Rodinia breakup. However, *Ge et al*. [2014a] proposed a continental arc-back-arc rifting setting based on the dominance of calc-alkaline granitoids and the conspicuous arc-like geochemical features of the mafic rocks.

Neoproterozoic regional metamorphism and deformation are well documented in the Aksu area, northwestern Tarim (Figure 1b). Here the blueschist-bearing Aksu Group was metamorphosed at high-pressure/low-temperature (HP/LT) conditions (up to 10 kbar, 300–400°C) [e.g., *Liou et al*., 1989, 1996; *Nakajima et al*., 1990; *Zhang et al*., 1999] and unconformably overlain by late Neoproterozoic clastic successions with Marinoan-aged glacial diamictites, basal conglomerates, and basalt interlayers[e.g., *Xu et al*., 2013; *He et al*., 2014b; *Wen et al*., 2015], providing strong evidence for a pre-635 Ma oceanic subduction and accretionary orogenic event in the northern Tarim Craton. Recent $^{39}Ar/^{40}Ar$ [*Yong et al*., 2012] and detrital zircon [*Zhu et al*., 2011a] dating indicate that the HP/LT metamorphism probably occurred at ca. 750–700 Ma, although precise dates have yet to be determined, and different interpretations of an older subduction and metamorphism exist [e.g., *Zhang et al*., 2012a].

The Korla area is located at the northernmost margin of the Tarim Craton adjacent to the South Tianshan Suture (Figures 1b and 1c). The area contains a suite of Neoarchean to early Paleoproterozoic (2.71–2.30 Ga) metamorphic rocks (i.e., the Korla Complex) consisting of orthogneiss, amphibolite, gneissic granitoids, and minor marble and mica schist in the north and a succession of late Paleoproterozoic (2.05–1.94 Ga) metasedimentary rocks (i.e., the Xingditag Group) including mica schist, paragneiss, marble, amphibolite, and minor quartzite and calc-silicate rock in the south [*Long et al*., 2010; *Dong et al*., 2011; *Zhang et al*., 2012b; *He et al*., 2013; *Ge et al*., 2013a, 2013b, 2014b]. All these rocks were metamorphosed to upper amphibolite facies and migmatized in the north at 1.8–1.9 Ga [e.g., *Ge et al*., 2013a, 2013b] and were intruded by ca. 830–800 Ma, 660–630 Ma, and 420 Ma massive granitoids [*Ge et al*., 2012a, 2012b, 2014a; *Guo et al*., 2013] as well as 660–630 Ma mafic dykes [*Zhu et al*., 2008, 2011b].

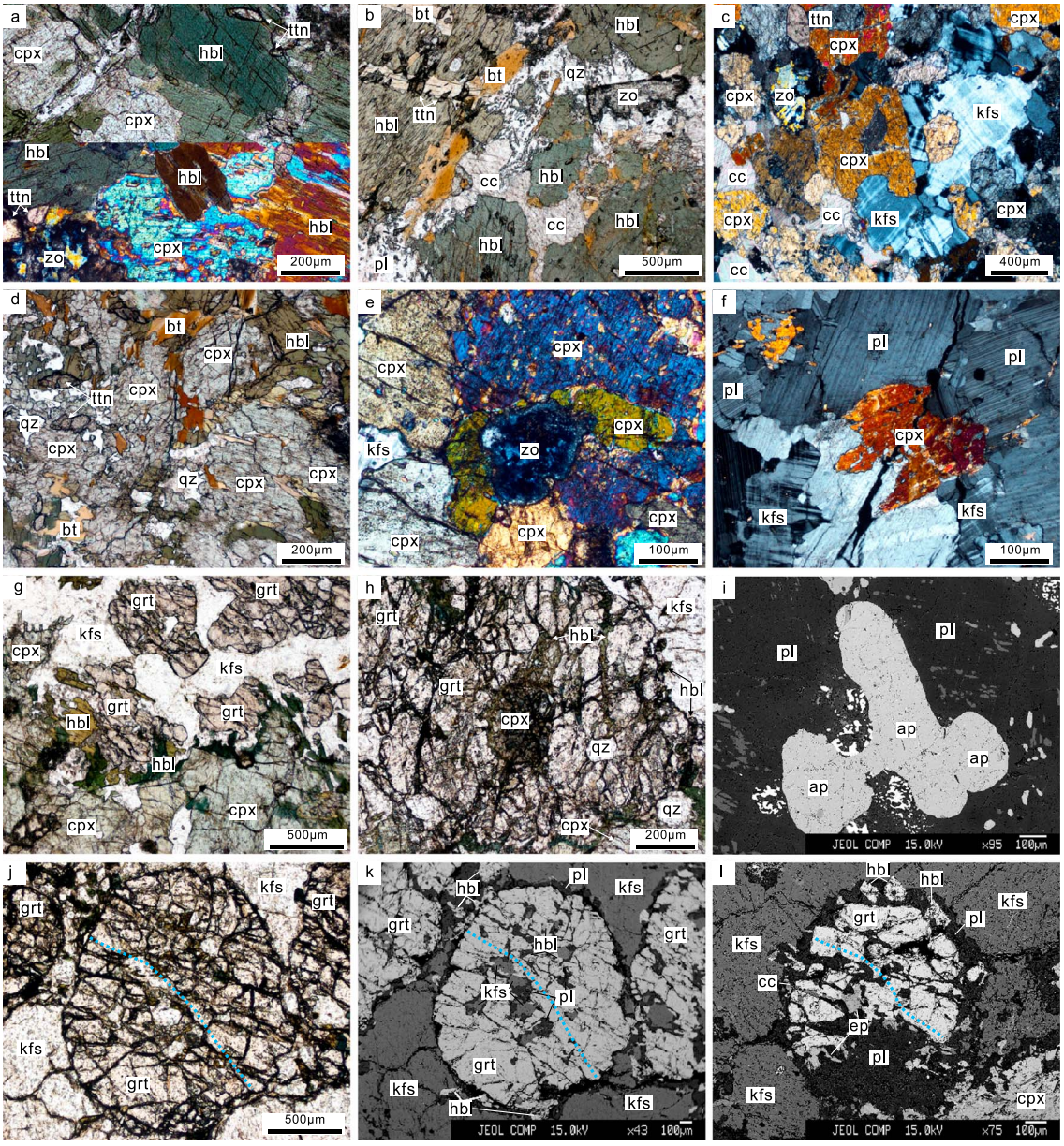

Figure 3. Photomicrographs showing the mineral assemblages and textures of representative rocks. (a) amphibolite; (b) calcite-bearing amphibolite; (c) calc-silicate rock; (d) pyroxenite; (e) zoisite in pyroxenite (sample 11K17); (f) peritectic clinopyroxene in leucogranite; (g) garnet pyroxenite (sample 11K17); (h) garnet porphyroblast containing clinopyroxene and quartz inclusions (sample 11K17); (i) SEM image showing large crystals of apatite (sample 12K24); (j) garnet porphyroblast analyzed by electron microprobe (sample 11K17); (k) SEM image of (j); (l) garnet porphyroblast analyzed by electron microprobe (sample 12K24). The dotted lines in Figures 3j–3l represent the composition profiles shown in Figures 5e and 5f. Note the occurrence of hornblende along cracks and rims of garnet and clinopyroxene in Figures 3g and 3h. Also, note the symplectite of hbl + pl ± ep ± cc after garnet in Figures 3k and 3l. Mineral abbreviations after *Whitney and Evans* [2010]: ap, apatite; bt, biotite; cc, calcite; cpx, clinopyroxene; ep, epidote; grt, garnet; hbl, hornblende; kfs, K-feldspar; pl, plagioclase; qz, quartz; ttn, titanite; zo, zoisite.

3. Field Relationships and Petrography

The high-grade mafic and calc-silicate rocks investigated here are from the southern part of the Korla area (Figure 1c). They occur as dark-colored boudins or lenses in the late Paleoproterozoic metasedimentary rocks, which comprise marble, mica schist, paragneiss, and minor quartzite (Figures 1d, 2a, and 2b). The host rocks are dominantly impure marble (Figures 2a and 2b) containing variable amount of muscovite, tremolite, serpentine, biotite, feldspar, and quartz. Some boudins are also found in mica schist. These boudins are a few centimeters to several meters wide and show variable length-to-width ratios. The contact between the boudins and the host rocks is generally distinct, but transitional contact between calc-silicate boudins and

Table 1. Summary of Mineral Assemblages and Zircon U-Pb Ages of the Mid-Neoproterozoic High-Grade Metamorphic Rocks in the Korla Area, Northern Tarim Craton

Sample	GPS Position	Lithology	Mineral Assemblage[a]	Zircon U-Pb Age[b] (Ma)
11K10	41°45′41.30″N 86°16′05.56″E	amphibolite	Hbl + Cpx + Bt + Pl + Qz, minor Zo + Ep + Ttn + Cc	823 ± 9
11K14	41°45′41.30″N 86°16′05.56″E	amphibolite	Hbl + Cpx + Zo + Bt + Pl + Qz, minor Ep + Ttn + Cc	1859 ± 10 826 ± 10
11K17	41°45′52.11″N 86°16′20.09″E	garnet pyroxenite	Cpx + Kfs + Grt + Hbl + Qz + Bt + Zo + Ap + Ttn	1735 ± 20 822 ± 17
11K33	41°45′39.50″N 86°16′04.06″E	amphibolite	Hbl + Cpx + Bt + Pl + Qz, minor Ep + Zo + Ttn + Cc	827 ± 11
11K36	41°45′40.47″N 86°16′04.15″E	calc-silicate rock	Hbl + Cpx + Bt + Cc + Qz + Zo + Pl, minor Ttn + Ep + Ilm	837 ± 7
11K38	41°45′44.94″N 86°16′10.48″E	amphibolite	Hbl + Cpx + Zo + Pl + Qz, minor Ttn + Ep + Ilm + Cc	1882 ± 27 831 ± 6 633 ± 16
11K40	41°45′44.94″N 86°16′10.48″E	amphibolite	Hbl + Cpx + Zo + Pl + Qz, minor Cc + Ttn + Ep	828 ± 8
12K24	41°46′05.31″N 86°17′02.24″E	garnet clinopyroxene gneiss	Pl + Kfs + Qz + Cpx + Bt + Grt + Hbl + Zo + Ap, minor Ttn + Ep + Cc	805 ± 13
13K49	41°47′36.76″N 86°13′52.98″E	garnet-bearing pyroxenite	Cpx + Ep + Ttn + Hbl + Grt + Pl + Qz, minor Kfs + Ap + Ilm +C c	820 ± 13
13K57	41°46′05.31″N 86°17′02.04″E	migmatite	melanosome: Cpx + Hbl + Bt + Kfs + Qz + Zo + Ep leucosome: Kfs + Qz + Pl + Cpx	831 ± 18
15K03	41°48′08.77″N 86°14′02.07″E	calc-silicate rock	Cc + Grt + Kfs + Hbl + Bt + Qz + Pl + Cpx + Zo, minor Ep + Ttn + ilm	809 ± 13
15K10	41°47′23.17″N 86°11′09.89″	biotite-garnet-K-feldspar gneiss	Grt + Kfs + Qz + Bt + Hbl, minor Ep + Zo + Cc + Ttn	807 ± 9

[a]Minerals are ordered with decreasing modal abundance. Ap, apatite; Bt, biotite; Cc, calcite; Cpx, clinopyroxene; Ep, epidote; Grt, garnet; Hbl, hornblende; Ilm, ilmenite; Kfs, K-feldspar; Pl, plagioclase; Qz, quartz; Ttn, titanite; Zo, zoisite.
[b]Weighted mean ages with 2σ.

impure marble is locally observed. These mafic and calc-silicate boudins are aligned subparallel to the main foliation that trends nearly E-W and dips subvertically (Figures 1d and 1e). Some of them show asymmetric σ-or domino-like structures, indicating near-horizontal dextral ductile shearing (Figure 2b).

Lithologically, these dark boudins are dominated by amphibolite containing abundant hornblende with variable amounts of biotite, clinopyroxene, garnet, plagioclase, quartz, K-feldspar, zoisite, titanite, and calcite (Figures 3a and 3b). Clinopyroxene locally exceeds hornblende and the rock grades into pyroxenite (Figures 3d and 3e). Feldspars locally reach 50%, and the rock is thus a mafic gneiss. Calcite with similar grain size and straight grain boundaries to the other minerals is found in a few samples (Figures 3b and 3c). Rocks with $>$5% calcite are identified as calc-silicate in this study. Euhedral to subhedral titanite and zoisite are present in most samples (Table 1). Garnet is absent in most samples and is only found in a few rocks, including amphibolite, pyroxenite, gneiss, and calc-silicate rocks. The modal contents of garnet locally exceed 10% (see below). Large euhedral apatite is found in some pyroxenites and mafic gneisses (Figure 3i). Patchy or banded leucosomes and leucogranitic veins, ranging in width from a few millimeters to tens of centimeters, are associated with pyroxenite at the northern end of the measured section (Figures 1d and 2d). Peritectic clinopyroxene is present in the leucosomes and leucogranitic veins (Figure 3f), indicating in situ partial melting under high-temperature conditions.

4. Whole-Rock Geochemistry

Whole-rock major and trace elements analyses were carried out for 23 samples, including amphibolite, pyroxenite, mafic gneiss, and calc-silicate rocks. The analytical methods are presented in Text S1 (supporting information), and the results are presented in Table S1 (supporting information).

The results indicate that these samples have variable major and trace element concentrations (Table S1). They are characterized by high CaO (11.6–22.2 wt %, average 17.0 wt %) and Sr (220–1361 ppm, average

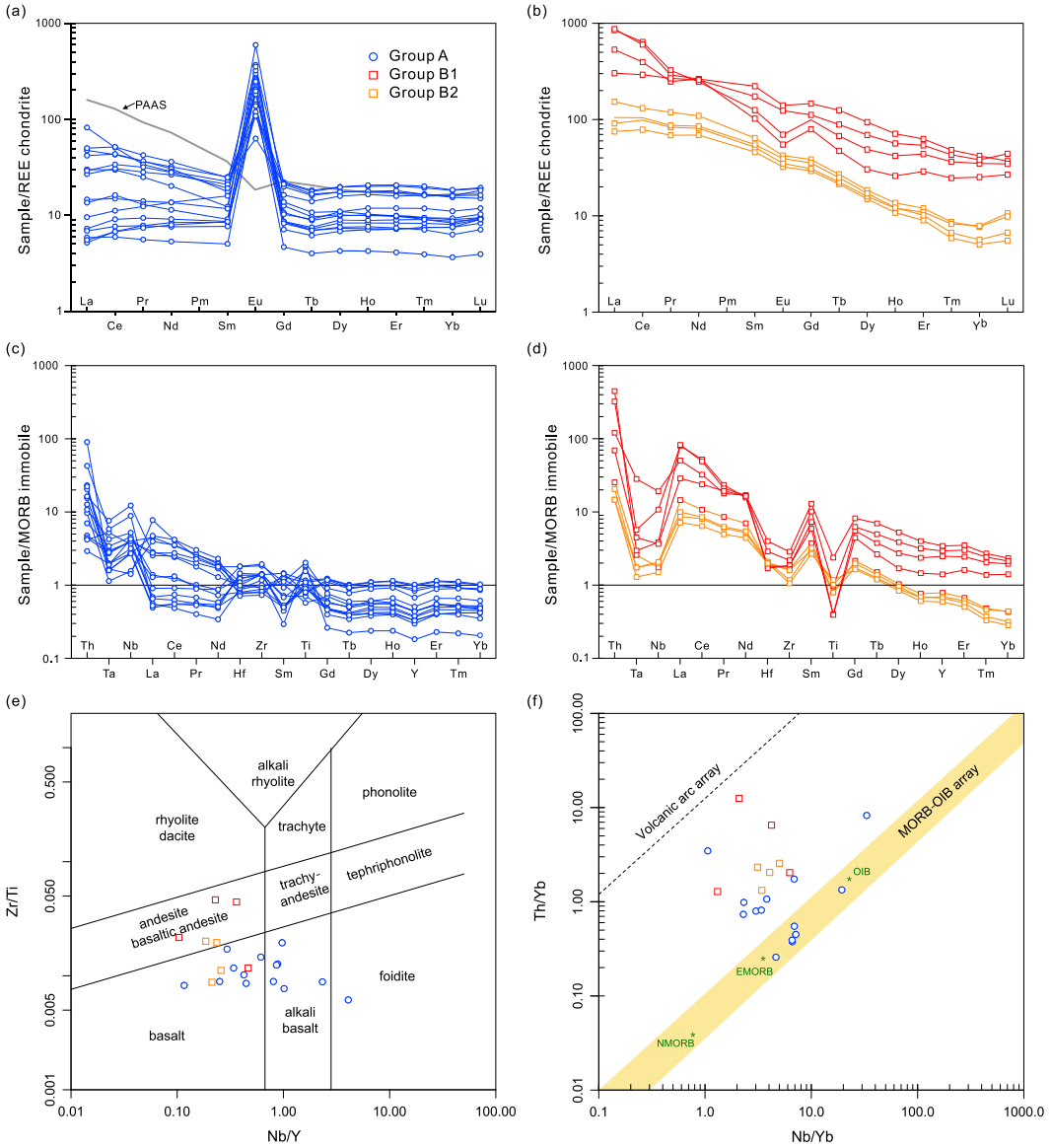

Figure 4. (a, b) REE and (c, d) trace element patterns; (e) Zr/Ti versus Nb/Y classification diagram [after *Pearce*, 1996]; and (f) Th/Yb versus Nb/Yb discrimination diagram [after *Pearce*, 2008] for the studied high-grade metamorphic rocks. Normalization values of REE chondrite and NMORB are from *Sun and McDonough* [1989].

608 ppm) and low Al_2O_3 (7.0–18.0 wt %, average 11.7 wt %) relative to common mafic igneous rocks (Table S1). Some samples also contain high P_2O_5 (1.0–2.2 wt %). The $Fe_2O_3^T$, TiO_2, Na_2O, and K_2O contents are also variable but show no systematic correlations with SiO_2 or Mg# (figures not shown).

According to rare earth element (REE) abundance and patterns, these samples can be classified into two groups. Group A samples have low total REE (21.0–109 ppm), relatively flat light REE (LREE) to heavy REE (HREE) ratios (normalized La/Yb = 0.5–4.5), and striking positive Eu anomalies (Eu* = 2.8–36.6, Table S1 and Figure 4a). In contrast, Group B samples are characterized by high REE abundance, fractionated LREE to HREE ratios (normalized La/Yb = 7.9–34.5), and weak negative Eu anomalies (Eu* = 0.61–0.89, Table S1 and Figure 4b). Four samples of Group B (Subgroup B1) show higher total REE contents (495–814 ppm) and lower $(Gd/Yb)_N$ ratios (2.8–3.5) than the others (Subgroup B2, total REE = 127–163 ppm, $(Gd/Yb)_N$ = 3.9–6.3, Table S1 and Figure 4b). Group B samples show marked negative Nb-Ta, Zr-Hf, and Ti anomalies, which are not present for Group A samples (Figures 4c and 4d).

5. Mineral Geochemistry and Phase Diagram Modeling

Two samples with high modal amounts of garnet and well-preserved mineral assemblages, a garnet pyroxenite (11K17) and a garnet clinopyroxene gneiss (12K24), are selected for detailed metamorphic petrology study and phase diagram modeling. Modal mineral contents are determined by point counting, and mineral compositions are determined by electron microprobe analyses (Text S1). The results are presented in Table S2 (supporting information).

Sample 11K17 is a garnet pyroxenite composed of 50% (volume percent) clinopyroxene, 17% k-feldspar, 13% garnet, 8% hornblende, 3% quartz, 2% plagioclase, 2% biotite, 2% zoisite, 2% apatite, and 1% titanite. The mineral assemblage records three stages of metamorphism. The first (prograde) stage is represented by the cpx + pl + kfs + qz + ttn assemblage (mineral abbreviations after *Whitney and Evans* [2010]) occurring as mineral inclusions in garnet porphyroblasts. The second (peak) stage is represented by the cpx + grt + kfs + bt + zo + qz + ttn + ap assemblage in the matrix. Note that plagioclase is absent in the matrix and zoisite is not found in garnet. The third (retrograde) stage is represented by hbl + pl symplectites replacing garnet at the rims or along cracks, as well as hornblende coronas surrounding clinopyroxene.

Sample 12K24 is a garnet clinopyroxene gneiss composed of 42% plagioclase, 23% clinopyroxene, 8% garnet, 8% hornblende, 5% k-feldspar, 6% biotite, 2% quartz, 2% zoisite, 2% apatite, 1% titanite, and minor epidote and calcite. The garnet porphyroblasts are intensively regressed, and only two metamorphic stages can be recognized: a peak stage represented by the grt + cpx + bt + pl + kfs + qz + zo + ttn + ap assemblage in the matrix and a retrograde stage represented by pl + hbl ± ep ± cc symplectites replacing garnet and hornblende coronas surrounding clinopyroxene.

Electron microprobe analysis indicates that the clinopyroxene is diopside (Table S2 and Figure 5a) in both samples. K-feldspar is mostly close to orthoclase (Or = 92.3–94.5, Table S2 and Figure 5b). No low-temperature ordered K-feldspar ($2V > 75°$) is observed. An contents of plagioclase are in the range of 25.3–39.9 for the symplectitic plagioclase in sample 11K17 and are 21.8–24.6 for plagioclase in the matrix and symplectite in sample 12K24 (Table S2 and Figure 5b). Amphibole belongs to the Ca group and is classified as hastingsite or ferropargasite in both samples (Table S2 and Figure 5c). Biotite also has similar compositions in the two samples (Table S2 and Figure 5d). Garnets are dominated by grossular and almandine, but they show different compositional zoning in the two samples. There is a slight increase in pyrope and decrease in spessartine from core to rim, whereas grossular and almandine show little variation in sample 11K17, consistent with prograde growth zoning (Figure 5e) [e.g., *Kohn*, 2003]. In contrast, garnets in sample 12K24 have been strongly retrograded and show a slight decrease in pyrope and increase in spessartine accompanied by a decrease in almandine and an increase in grossular from core to rim (Figure 5f), implying diffusion and/or resorption during retrograde metamorphism [e.g., *Kohn*, 2003].

Phase diagram modeling is carried out in the MnNCKFMASHT system using Perple_X (v6.6.7) [*Connolly*, 2005] and the internally consistent thermodynamic database (hp02ver.dat) [*Holland and Powell*, 1998]. The solution models of Gt(WPH) [*White et al*., 2007], Omph(GHP2) [*Diener and Powell*, 2012], cAmph(DP2) [*Diener and Powell*, 2012], feldspar [*Fuhrman and Lindsley*, 1988], Kf [*Waldbaum and Thompson*, 1968], O (HP) [*Holland and Powell*, 1998], Bio(TCC) [*Tajčmanová et al*., 2009], Mica(CHA) [*Auzanneau et al*., 2010], Ilm(WPH) [*White et al*., 2007], and Neph(FB) [*Ferry and Blencoe*, 1978] were used to calculate the stability fields of garnet, clinopyroxene, amphibole, high-temperature K-feldspar and plagioclase, low-temperature K-feldspar, olivine, biotite, muscovite, ilmenite, and nepheline, respectively. Quartz, titanite, zoisite, rutile, and water are assumed to be pure phases. Melt is not included in order to simplify calculation because partial melting is limited in the modeled samples. The effective bulk compositions are taken from X-ray fluorescence analyses (Table S1). The CaO contents have been corrected for apatite assuming that all P_2O_5 is hosted in apatite with an average composition of 56 wt % CaO, 42 wt % P_2O_5, and 2 wt % F (Table S2). CO_2 and O_2 are ignored because carbonate and Fe^{3+}-bearing minerals (e.g., epidote) are insignificant in the studied samples. Water contents are assumed to equal Loss on Ignition (LOI), i.e., 0.51 and 0.41 wt % for samples 11K17 and 12K24, respectively (Table S1). The latter is probably too low because it is unable to stabilize amphibole for the effective bulk composition of sample 12K24. Thus, a slightly increased water content (0.5 wt %) is used in the calculation. Calculated *T-X*(H_2O) and *P-X*(H_2O) sections (unpublished) indicate that higher water contents (>0.7 wt %) stabilize amphibole at low-*T* and high-*P* conditions but have little influence on the stabilities of other phases.

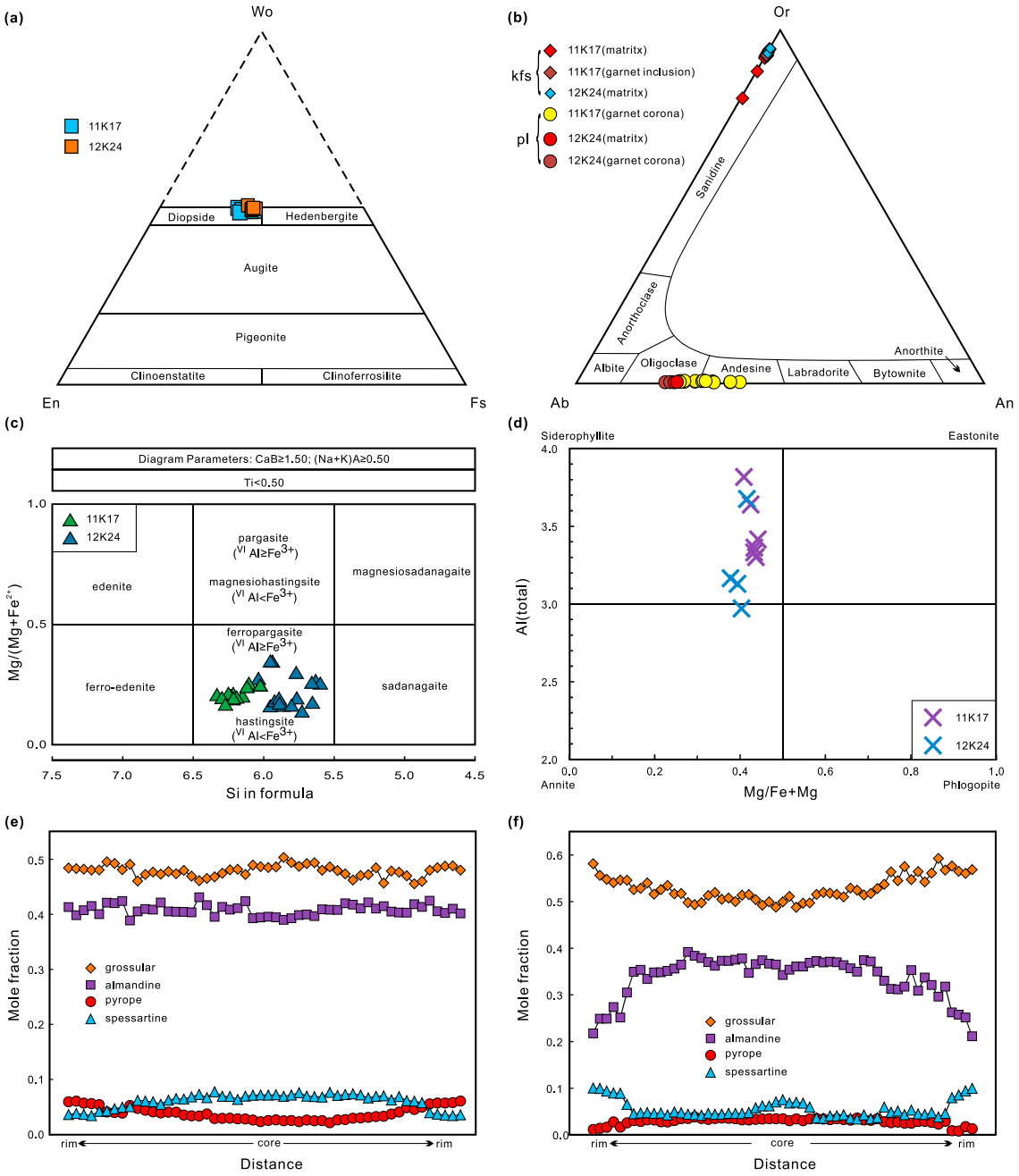

Figure 5. (a) Wo-En-Fs classification diagram for clinopyroxene; (b) Or-Ab-An classification of feldspar; (c) Mg/(Mg + Fe^{2+}) versus formula Si classification diagram for amphibole; (d) total Al versus Mg/(Mg + Fe) classification diagram for biotite; (e) composition profile of garnet porphyroblast in sample 11K17; (f) composition profile of garnet porphyroblast in sample 12K24. Profile locations for Figure 5e are shown in Figures 3j and 3k, and for Figure 5f in Figure 3l.

Figure 6a is the calculated *P-T* pseudosection for sample 11K17. It is dominated by regions with three to five variances. Clinopyroxene, biotite, and titanite are stable in the entire modeled *P-T* range. K-feldspar is also stable in the entire diagram, but there is a transition from high-temperature state to low-temperature state at ~460°C. Garnet is replaced by olivine in the high-*T*/low-*P* region. Plagioclase disappears above 8–12 kbar and becomes immiscible below ~550°C and 5.5 kbar. Muscovite (or phengite) becomes stable at relatively high-*P* (>7.5 kbar) and low-*T* (<780°C) conditions instead of zoisite. The observed peak and retrograde mineral assemblages are stable in two small areas at 620–730°C, 10–13 kbar and 460–500°C, 3–5 kbar, respectively, but the prograde assemblage is stable over a large *P-T* range. The relevant regions are contoured in Figure 6a with the calculated pyrope and grossular fractions in garnet. The pyrope content in garnet increases

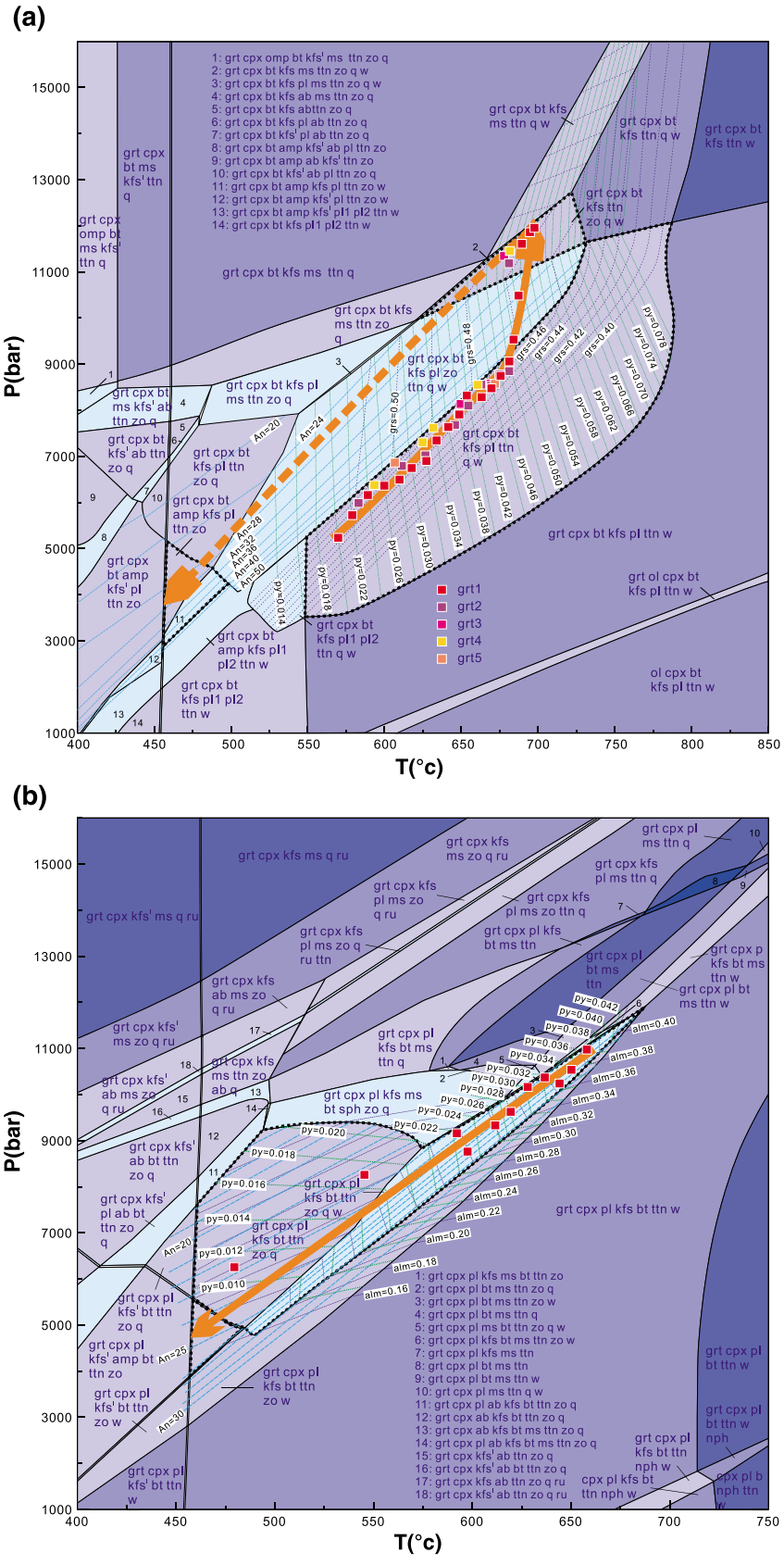

Figure 6

with increasing temperature, whereas the grossular and An contents vary with both temperature and pressure. The average measured pyrope and grossular contents of five garnet porphyroblasts are plotted in Figure 6a. The results show that the garnet cores and mantles record a prograde *P-T* path from 570°C and 5.2 kbar to 680°C and 9.0 kbar, whereas the garnet rims record a peak metamorphic condition at 680–700°C and 11.2–12.0 kbar. The latter is consistent with the optimal *P-T* (699 ± 41°C, 12.1 ± 1.3 kbar, cor = 0.861, σ_{fit} = 1.28) given by the average *P-T* approach in THERMOCALC [*Powell and Holland*, 1994] and the temperatures (680–710°C) given by the garnet-clinopyroxene thermometer [e.g., *Berman et al*., 1995; *Ganguly et al*., 1996]. The *P-T* condition of the retrograde stage is constrained at 460–500°C and 3–5 kbar according to the mineral assemblage and the An contents of coronal plagioclase. These results thus define a counterclockwise *P-T* path for sample 11K17 (Figure 10).

The calculated *P-T* pseudosection for sample 12K24 (Figure 6b) is also dominated by regions with three to five variances. Clinopyroxene is present in the entire modeled *P-T* range. Garnet is replaced by nepheline in the low-*P*/high-*T* corner. Titanite is replaced by rutile under high-*P*/low-*T* condition. Muscovite becomes the water-bearing phase in the high-*P*/low-*T* fields instead of biotite and zoisite. The transition from high to low K-feldspar also occurs at ~460°C, but the plagioclase solvus does not appear. The peak mineral assemblage is stable in two large fields with or without water. The pyrope fraction increases with increasing temperature in the water-present field but increases with increasing pressure in the water-absent field. The almandine fraction is more sensitive to *P-T* change than grossular in these two regions and is contoured in Figure 6b to constrain *P-T* conditions, combined with the An isopleth. The highest pyrope fraction in a garnet core and An contents of matrix plagioclase record a peak metamorphic condition of ~660°C, 11.0 kbar, which is consistent with the optimal *P-T* (672 ± 51°C, 12.0 ± 1.9 kbar, cor = 0.864, σ_{fit} = 1.66) given by THERMOCALC and the temperatures (630–670°C) given by the garnet-clinopyroxene thermometers [e.g., *Berman et al*., 1995; *Ganguly et al*., 1996]. The compositions of garnet mantle and rim plot on a retrograde path, but the uncertainty is large due to resorption and/or diffusion during retrograde metamorphism [*Kohn*, 2003] and subparallel isopleths for pyrope and almandine. The retrograde assemblage is restricted to a small region at 460–480°C, 4.0–5.0 kbar, which is consistent with the An contents of plagioclase in the garnet coronas.

6. Zircon U-Pb Ages, Hf Isotopes, and Trace Elements

In situ zircon U-Pb dating using laser ablation-inductively coupled plasma mass spectrometry (LA-ICPMS) was carried out for 12 samples. Most of these samples were also analyzed for Lu-Hf isotopes and trace elements. The analytical methods and results are presented in Text S1 and Tables S3–S5 (supporting information).

Cathodoluminescence (CL) images reveal that most zircons or zircon domains can be classified into two groups: Group I zircons are CL-dark anhedral grains or cores with homogeneous internal structure, or patchy to blurred oscillatory zoning (Figures 7f to 7j); Group II zircons are CL-bright grains or overgrowth rims with patchy zoning or homogeneous internal structures (Figures 7a to 7f), suggesting a possible metamorphic origin. Group I zircons are found only in a few samples (11K10, 11K14, 11K17, 11K38, 13K57, 15K03, and 15K10), whereas Group II zircons are present in all samples and are dominant in some samples (11K33, 11K36, 11K40, and 12K24). Group II zircons from sample 13K49 are overgrown by CL-grey rims with homogeneous internal structures (Group II′, Figure 7e). In addition, several euhedral zircons with well-developed oscillatory zoning (Group III) are also found in sample 11K38 (Figure 7j).

Figure 6. *P-T* pseudosections for (a) sample 11K17 and (b) sample 12K24 calculated using Perple_X. The effective bulk compositions are SiO_2 = 47.64%, TiO_2 = 0.5%, Al_2O_3 = 7.01%, FeO = 11.61%, MnO = 0.43, MgO = 6.42%, CaO = 16.95%, Na_2O = 0.99%, K_2O = 1.64%, and H_2O = 0.51% for sample 11K17, and SiO_2 = 51.28%, TiO_2 = 0.47%, Al_2O_3 = 15.17%, FeO = 7.59%, MnO = 0.30, MgO = 2.99%, CaO = 10.58%, Na_2O = 4.11%, K_2O = 1.54%, and H_2O = 0.50% for sample 12K24. All in weight percent. Thick dotted lines outline the observed mineral assemblages. The related regions are contoured with pyrope (py) and grossular (grs) or almandine (alm) fractions of garnet, and the An fraction of plagioclase. The average compositions of garnet porphyroblasts in the two samples are plotted. Thick arrowed lines represent inferred *P-T* paths. Mineral abbreviations: amp, amphibole; bt, biotite; cpx, clinopyroxene; grt, garnet; ilm, ilmenite; kfs, high-temperature K-feldspar; kfs^l, low-temperature K-feldspar; ms, muscovite; nep, nepheline; ol, olivine; pl, plagioclase; q, quartz; ru, rutile; ttn, titanite; w, water; zo, zoisite.

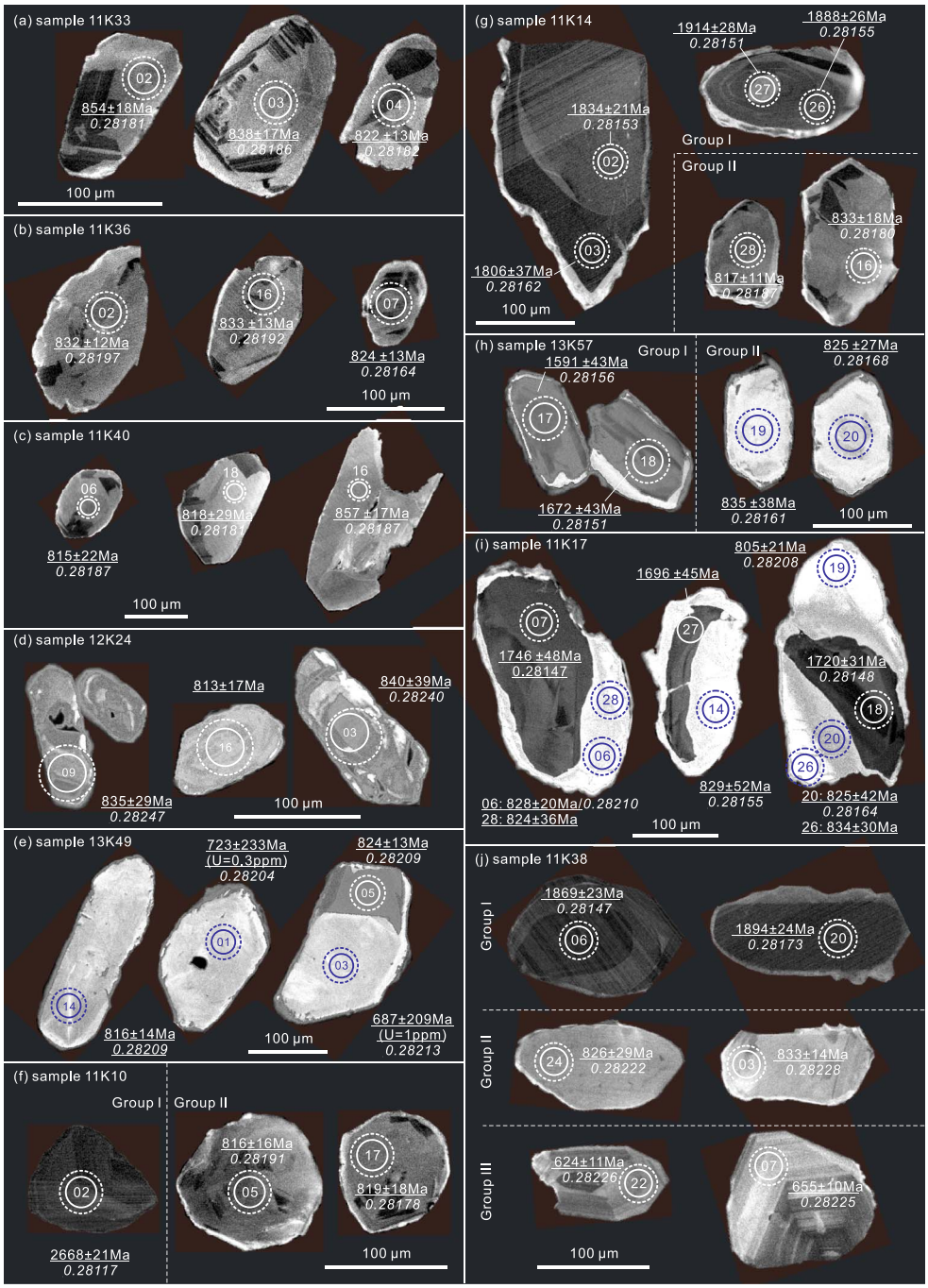

Figure 7. Typical CL images of zircon grains from the mid-Neoproterozoic high-grade metamorphic rocks in the Korla area. Solid circles represent U-Pb dating site with a diameter of ~30 μm, whereas the dotted circles represent Lu-Hf analysis site with a diameter of ~44 μm. The numbers in the solid circles are the analysis number for each sample. $^{206}Pb/^{207}Pb$ (>1000 Ma) or $^{206}Pb/^{238}U$ (<1000 Ma) ages with 1σ error are underlined, whereas the initial $^{176}Hf/^{177}Hf$ values are shown in italic. Note the presence of multiple zircon domains in Figures 7e–7j. See text for interpretation of Group I, II, and III zircons.

LA-ICPMS U-Pb analyses show that the Group I zircons mostly have moderate Th (average 136 ppm) and U (average 425 ppm) contents and moderate Th/U ratios (average 0.34, Table S3 and Figures 9a and 9b). Except for a few outliers, most analyses yield concordant ages between 2.0 and 1.6 Ga (Table S3), with weighted mean $^{206}Pb/^{207}Pb$ ages ranging from 1882 ± 38 Ma to 1731 ± 59 Ma (Figure 8), indicating a late Paleoproterozoic tectonothermal event. In contrast, the Group II zircons mostly contain <15 ppm Th

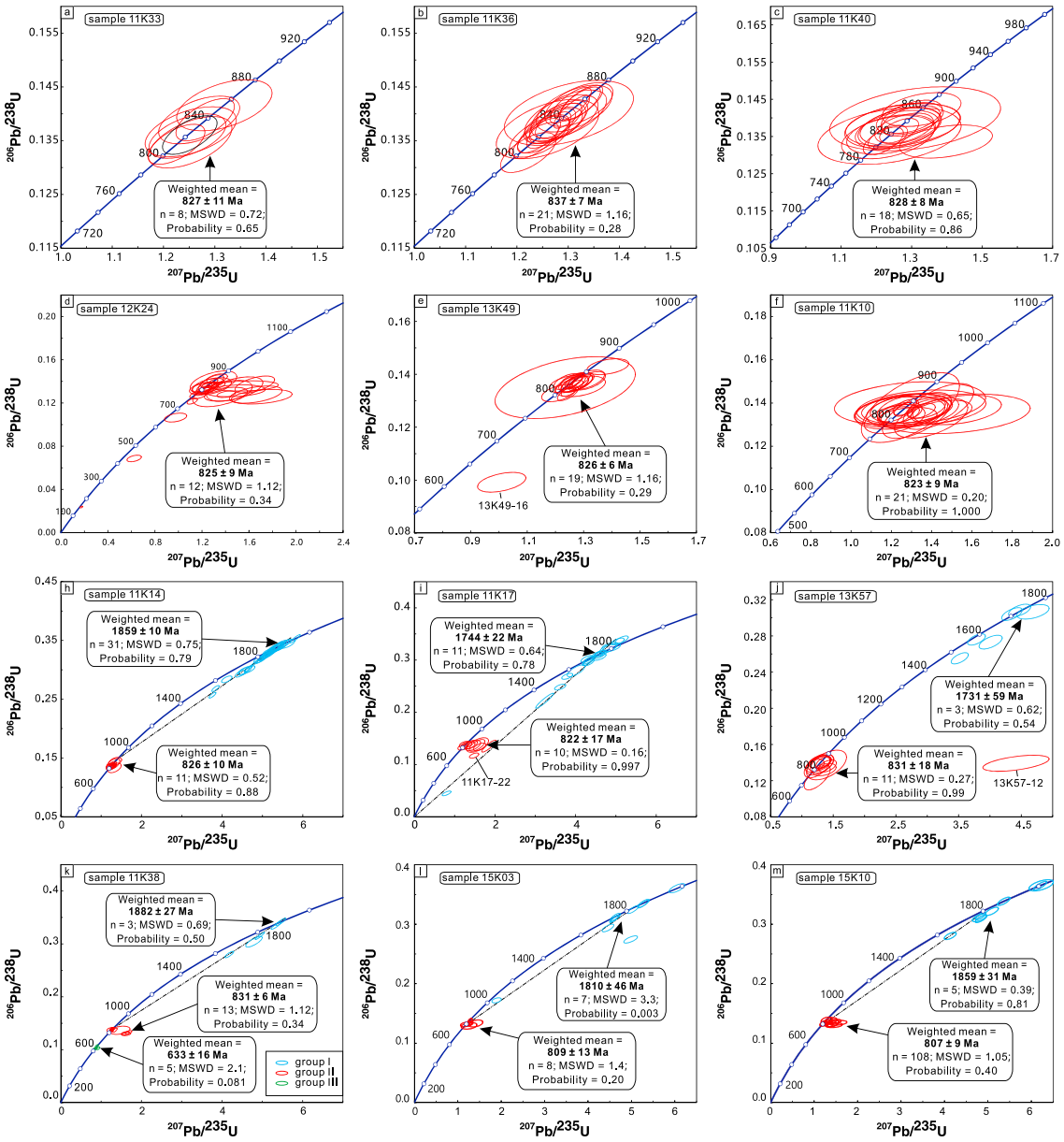

Figure 8. Zircon U-Pb concordia diagrams for the mid-Neoproterozoic high-grade metamorphic rocks in the Korla area, northern Tarim Craton.

(average 2.0 ppm) and <150 ppm U (average 97 ppm) and have low Th/U ratios (<0.1, average 0.05, Table S3 and Figures 9a and 9b). They mostly yield concordant or nearly concordant ages around 830–800 Ma, with weighted mean $^{206}Pb/^{238}U$ ages between 837 ± 7 Ma and 807 ± 9 Ma (Figure 8). Group II zircons from sample 13K49 have extremely low U contents (<1 ppm, Table S3) and consequently were unable to yield precise U-Pb ages. However, the CL-grey overgrowth rims (Group II') have moderate U contents (10–256 ppm) and yield concordant ages with a similar weighted mean $^{206}Pb/^{238}U$ age of 826 ± 6 Ma (Figure 8e). These age data suggest that all the studied samples were metamorphosed in the mid-Neoproterozoic (ca. 830–800 Ma). In addition, five analyses on Group III zircons from sample 11K38 yield high Th/U ratios and near-concordant ages around 633 ± 16 Ma (Figure 8k), probably recording late Neoproterozoic melt/fluid infiltration.

LA-MC-ICPMS Lu-Hf isotopic analyses indicate that the Group I zircons have a limited range of initial $^{176}Hf/^{177}Hf$ values (0.28153 ± 0.00009, 1σ, Table S4 and Figure 9c) except for a few outliers. This is consistent with the previous finding of relatively homogeneous initial Hf isotopic compositions for late Paleoproterozoic metamorphic zircons from mica schists in the same area [*Ge et al.*, 2013a]. In contrast, the

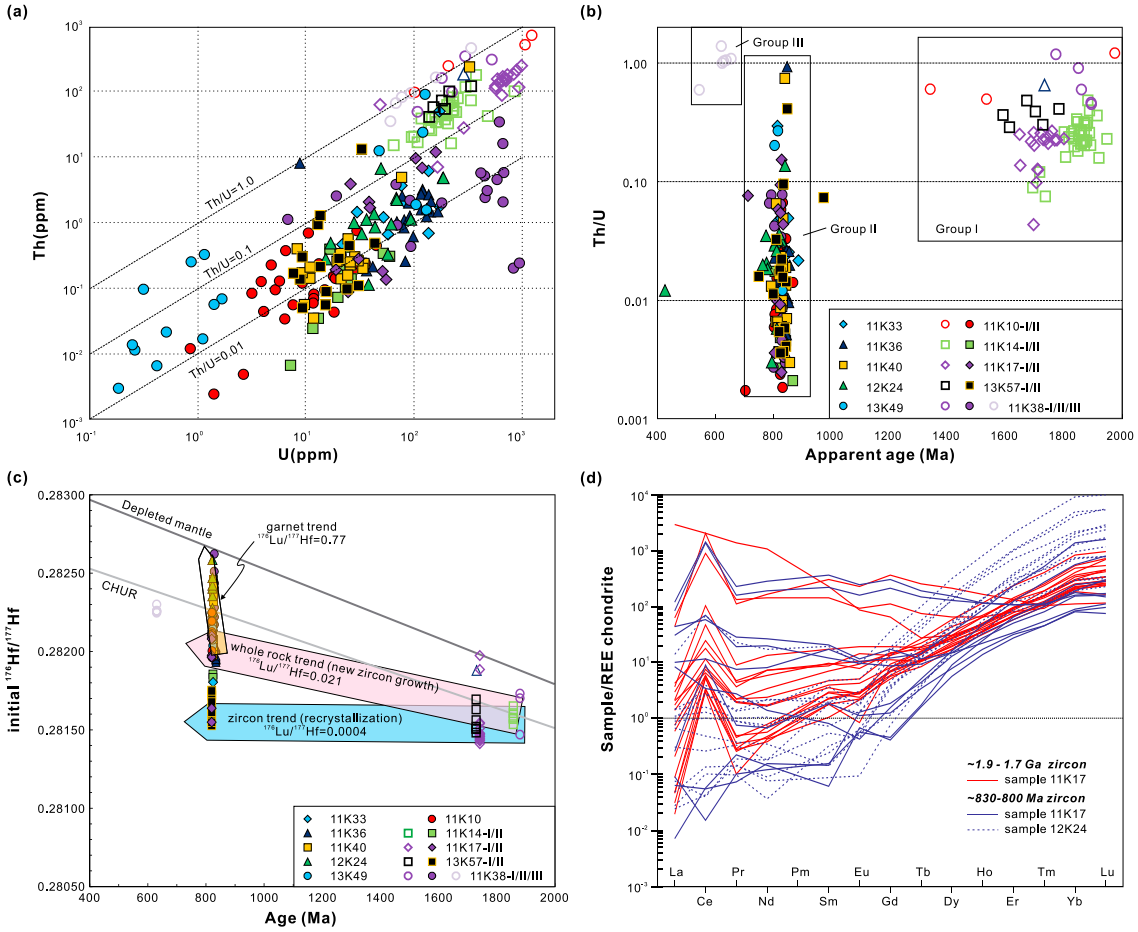

Figure 9. (a) Th versus U contents of the dated zircons (legend in Figure 9b). (b) Th/U versus apparent $^{206}Pb/^{238}U$ age (<1000 Ma) or $^{206}Pb/^{207}Pb$ age (>1000 Ma). Note the low Th, U contents, and Th/U ratios of the ca. 830–800 Ma metamorphic zircons. (c) Initial $^{177}Hf/^{176}Hf$ versus weighted mean age for zircons. The $^{177}Lu/^{176}Hf$ values for the zircon trend (0.004), whole-rock trend (0.021), and garnet trend (0.77) are estimated from average $^{177}Lu/^{176}Hf$ of all analyzed zircons, average whole-rock Lu/Hf ratios (0.15), and garnet Lu-Hf isotopic analysis (sample FTS 5-15) from *Klemd et al.* [2011], respectively. (d) Chondrite-normalized REE patterns of zircons from samples 11K17 and 12K24. Normalization values from *Sun and McDonough* [1989]. Note the steep HREE slopes and variable HREE contents, as well as Eu and Ce anomalies, for both ca. 1.9–1.7 Ga and ca. 830–800 Ma zircons.

ca. 830–800 Ma Group II zircons have more variable initial $^{176}Hf/^{177}Hf$ (0.28153–0.28262, Table S4 and Figure 9c). Their initial $^{176}Hf/^{177}Hf$ values are generally higher than those for the 1.9–1.7 Ga zircons, and there is a marked increase in initial $^{176}Hf/^{177}Hf$ values from the 1.9–1.7 Ga zircons to the ca. 830–800 Ma zircons when both zircon domains/groups were analyzed on the same grain (e.g., Figure 7i) or from the sample (e.g., Figures 7g, 7h, and 7j). This observation, combined with CL characteristics, suggests that the ca. 830–800 Ma zircons were formed through metamorphic growth or overgrowth, instead of in situ recrystallization of the 1.9–1.7 Ga zircons, because the latter process is unlikely to significantly increase the $^{176}Hf/^{177}Hf$ values [e.g., *Gerdes and Zeh*, 2009].

Zircon REE distribution patterns exhibit large variations for both ca. 1.9–1.7 Ga and ca. 830–800 Ma zircons (Figure 9d and Table S5). Some grains have significantly elevated LREE contents (normalized La/Yb > 0.1) relative to typical igneous zircons possibly due to micro-inclusions. Both positive and negative Ce* and Eu* anomalies are present in both zircon groups from most samples (Table S5). These characteristics are clearly different from zircons of igneous origin, which in turn supports a metamorphic origin for both groups of zircons. The slopes between HREEs are steep except for analyses with elevated LREE contents. This is also true for zircons from samples 11K17 and 12K24 that contain abundant garnet (Figure 9d).

Ti-in-zircon temperatures were calculated using the measured Ti contents and the calibrations given by *Watson et al.* [2006] and *Ferry and Watson* [2007]. Based on the presence of quartz and titanite (rather than

rutile) in the mineral assemblages, the activities of SiO_2 and TiO_2 are assumed to be 1 and 0.8, respectively, for the latter calibration. This yields Ti-in-zircon temperatures ~20°C higher than the *Watson et al*. [2006] calibration (Table S5). The ca. 830–800 Ma zircons yield average Ti-in-zircon temperatures of 669–689°C for sample 11K17 and 634–650°C for sample 12K24, slightly lower than the peak metamorphic temperatures obtained for these samples. The ca. 830–800 Ma zircons in other samples yield similar average Ti-in-zircon temperatures between 630 and 660°C, except for sample 11K14 which records lower average Ti-in-zircon temperatures (535–542°C, Table S5). In contrast, the 1.9–1.7 Ga zircons yield average Ti-in-zircon temperatures of 712–779°C, significantly higher than the peak metamorphic temperatures obtained above.

7. Discussion

7.1. Protolith and Petrological Implications

The high-grade metamorphic rocks investigated here have a broadly mafic mineral assemblage (amphibole and pyroxene) and whole-rock geochemical compositions (Table S1). However, compared to common mafic igneous rocks, these samples have unusually high CaO contents, as well as low Al_2O_3 and high P_2O_5 and Sr for some samples (Table S1). The high CaO contents are consistent with high modal abundance of Ca-rich minerals, including Ca-amphibole, diopside, and titanite, as well as grossular-rich garnet, zoisite, calcite, and apatite in some samples. Such a Ca-rich composition may suggest a sedimentary origin from impure sediments like calcareous shale or argillaceous carbonate, as has been proposed for some para-amphibolites [e.g., *Walker et al*., 1959; *Leake*, 1964]. A sedimentary origin of these rocks seems consistent with the close association with impure marble and mica schist and high modal abundance of calcite in some samples. A simple mixing calculation suggests that the average anhydrous composition of the studied samples can be matched by 60% PAAS (post-Archean Australia Shale [*Taylor and Mclennan*, 1985]) + 40% Fe-rich dolomite (~15 wt % $Fe_2O_3^T$, ~10 wt % MgO, and ~34 wt % CaO) for most major elements. However, such a pelite-carbonate mixture implies high contents of volatiles (~17 wt % CO_2) and carbonate minerals, which is inconsistent with the low LOI values (0.41–3.68 wt %) and the low modal amounts of calcite in most samples. Moreover, a sedimentary origin cannot explain the low total REE abundance and the striking positive Eu anomalies for Group A samples, because sedimentary rocks generally have elevated REE and negative Eu anomalies [e.g., *Taylor and Mclennan*, 1985]. The negative Zr-Hf anomalies in the mid-ocean ridge basalt (MORB)-normalized trace element diagrams for Group B samples (Figure 4b) are also difficult to explain for sedimentary rocks.

An alternative interpretation for the high CaO contents is metasomatism of mafic igneous rocks by Ca-rich fluids. This has been documented in many high pressure-ultrahigh pressure (HP-UHP) metamorphic terranes and may have been an efficient mechanism for the selective mobilization of major and trace elements from the subducting oceanic slab to overlying mantle wedge [e.g., *John et al*., 2008; *Beinlich et al*., 2010; *Klemd*, 2013]. For example, Ca-metasomatism in the South Tianshan has induced as much as 115% enrichment of CaO and 40–80% depletion of large ion lithophile element (LILE) and LREE in the altered oceanic basalts (eclogites) relative to unaltered blueschist [*John et al*., 2008; *Beinlich et al*., 2010]. Such an efficient enrichment of CaO and scavenging of LREE can interpret the high CaO and variably low REE in the Group A samples. Interestingly, *Beinlich et al*. [2010] demonstrated that the altered basalts show an enrichment of Eu, whereas other REEs are significantly depleted, which helps to explain the positive Eu anomalies in the Group A samples. The altered rocks also show a decrease in Al_2O_3 and increase in $Fe_2O_3^T$ [*Beinlich et al*., 2010], consistent with the relatively low Al_2O_3 and high $Fe_2O_3^T$ in the studied samples.

Therefore, we conclude that the high-grade rocks investigated here were probably derived from mafic igneous rocks, which may have been strongly altered in major and trace element compositions by influx of Ca-rich fluids. However, the trace elements of the Group B samples were probably less altered because they have high REE contents and consistent REE patterns (Figure 4b). Thus, we use REE and immobile high field strength elements (HFSE) of Group B samples to infer the attributes of the protolith. On the Zr/Ti versus Nb/Y diagram, the Group B samples plot in the basalt to andesite fields (Figure 4e). On the NMORB (normal mid-ocean ridge basalt) -normalized trace element diagram, they show marked enrichment in LREE and Th and depletion in Nb-Ta, Zr-Hf, and Ti (Figure 4d), which are typical for arc-related igneous rocks. On the Th/Yb versus Nb/Yb diagram, they plot above the MORB-OIB (oceanic island basalt) array but subparallel to the volcanic arc array(Figure 4f). These geochemical features indicate a parent magma composition similar to continental arc basalt [e.g., *Pearce*, 2008]. It is speculated that the parent magma possibly emplaced as

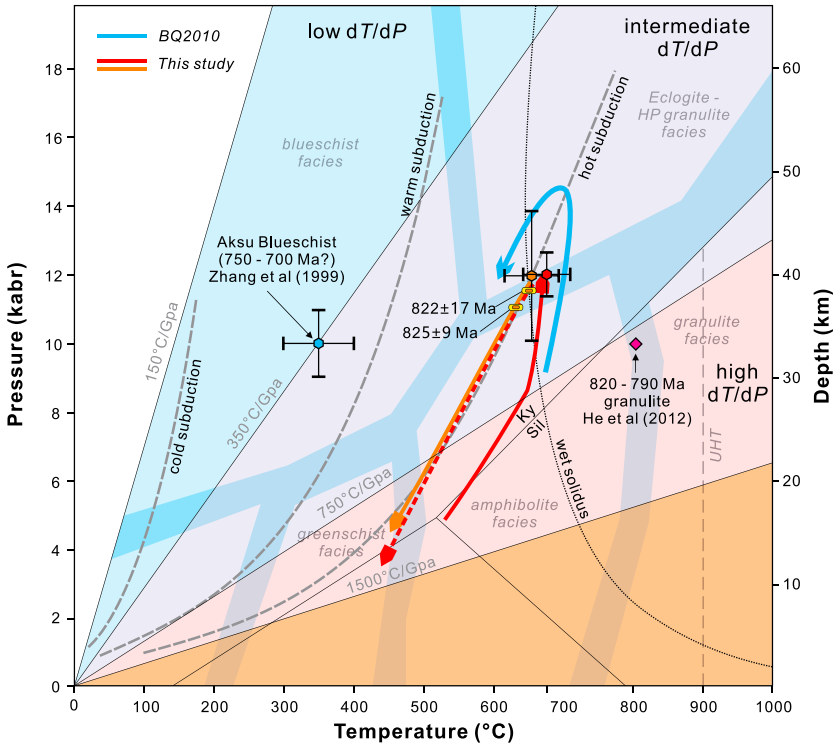

Figure 10. *P-T-t* paths of the mid-Neoproterozoic high-grade metamorphic rocks in northern Tarim Craton. The boundaries between metamorphic facies and low, intermediate, and high d*T*/d*P* type metamorphism are from *Brown* [2014]. The geothermal gradients for cold, warm, and hot subduction are from *Bhowmik and Ao* [2016]. Peak *P-T* conditions and errors of the two samples estimated using the average *P-T* approach in THERMOCALC are shown for comparison with the *P-T* path obtained using phase diagram modeling. Metamorphic zircon U-Pb ages are tied to the *P-T* path according to the average Ti-in-zircon temperatures in the two samples and probably date the early exhumation and cooling event shortly after peak metamorphism. The peak metamorphic conditions for the 820–790 Ma granulites [*He et al.*, 2012] and the 750–700 Ma Aksu blueschists [*Zhang et al.*, 1999] are also shown. The *P-T* path for a garnet amphibolite (BQ2010) from the La Corea mélange of eastern Cuba resulting from subduction onset of the young and hot proto-Caribbean oceanic plate [*Blanco-Quintero et al.*, 2010] is shown for comparison.

dykes or sills into Paleoproterozoic carbonate and clastic rocks in a continental arc setting and was later altered by Ca-rich fluids and dismembered into boudins during a later tectonothermal event. Due to a lack of igneous zircons from the protolith, the time of magma emplacement, fluid alteration, and deformation, as well as the relationship of these events with the Neoproterozoic metamorphism, need further studies in the future. Group A samples plot in diverse lithologies and tectonic settings in Figures 4e and 4f, but whether this results from metasomatic modification of these relatively immobile elements or reflects a more complex protolith history remains unclear.

7.2. *P-T-t* Path and Tectonic Setting

The two samples used for phase diagram modeling show well-preserved peak mineral assemblages, which do not change over the sample scale, suggesting that the alteration process mentioned above occurred on a large scale and before the high-grade metamorphism. Thus, the studied samples represent a closed system and are suitable for *P-T* calculations using phase diagram modeling. The results indicate that the garnet pyroxenite (11K17) experienced a prograde metamorphic stage from ~570°C and 5.2 kbar to ~680°C and 9.0 kbar, a peak metamorphic stage at 680–700°C and 11.2–12.1 kbar, and a retrograde metamorphic stage at 460–500°C and 3–5 kbar. There is a near-isothermal compression stage from ~680°C and 9.0 kbar to 680–700°C and 11.2–12.1 kbar. The garnet clinopyroxene gneiss (12K24) did not record the prograde stage metamorphism due to strong resorption of garnet porphyroblasts but recorded peak metamorphism at 660–670°C and 11.0–12.0 kbar and retrograde metamorphism at ~460–480°C and 4–5 kbar, consistent with sample 11K17. Collectively, these two samples record a consistent counterclockwise *P-T* path involving heating and burial, subsequent near-isothermal burial, and final cooling and exhumation (Figure 10).

The peak metamorphic conditions correspond to upper amphibolite to high-pressure granulite facies with an apparent geothermal gradient of ~18°C/km, consistent with intermediate d*T*/d*P* metamorphism (~10–20°C/km, Figure 10) [e.g., *Brown*, 2007, 2009, 2014]. This is distinct from the low d*T*/d*P* metamorphism with low apparent geothermal gradient (~5–10°C/km) registered by HP-UHP metamorphic rocks formed in mature oceanic subduction zones or during the early stages of continental collision. It is also distinct from the high d*T*/d*P* type metamorphism with high apparent geothermal gradient (~20–40°C/km) recorded by granulites and ultrahigh temperature (GUHT) metamorphic rocks that are usually found in crustal extensional settings or back arc to orogenic hinterland [*Brown*, 2007, 2009, 2014]. *Brown* [2007, 2009, 2014] suggested that the intermediate d*T*/d*P* type metamorphism, also referred to eclogite-high-pressure granulite metamorphism (EHPG), is related to subduction-to-collision settings, where some components (medium-temperature eclogite) are related to subduction but other components (high-pressure granulite) record crustal thickening in arcs. However, these high-pressure granulites and medium-temperature eclogites usually record clockwise *P-T* path involving near-isotherm decompression [*Brown*, 2007, and references therein], opposite to the counterclockwise *P-T* path involving near-isothermal compression documented above.

Counterclockwise *P-T* paths have been predicted by thermomechanical modeling during the initial stage of oceanic subduction [*Gerya et al*., 2002] and have been documented in the geological record in several subduction complexes worldwide, including the Franciscan Complex of California, the Coastal Cordillera accretionary complex of Chile, the Villa de Cura blueschist belt of Venezuela, and the Sierra del Convento and La Corea mélange of Cuba [*Bhowmik and Ao*, 2016, and references therein]. Compared to clockwise *P-T* paths commonly recorded by HP-UHP rocks, counterclockwise *P-T* paths are usually recorded by relatively high-grade rocks (e.g., garnet amphibolites) with higher temperature and lower pressure peak metamorphic conditions, corresponding to apparent thermal gradients as high as 14–16°C/km [e.g., *Blanco-Quintero et al*., 2010]. These rocks are commonly overprinted by blueschist facies retrograde metamorphism along near-isobaric cooling paths before final exhumation and cooling [*Bhowmik and Ao*, 2016, and references therein]. These are interpreted as recording relatively high geothermal gradient during subduction initiation and subsequent cooling of the subduction channel with ongoing subduction [e.g., *Gerya et al*., 2002; *Blanco-Quintero et al*., 2010; *Bhowmik and Ao*, 2016].

The peak metamorphic conditions and overall counterclockwise *P-T* path of the high-grade rocks in this study are similar to those recorded by garnet amphibolites in the La Corea mélange of eastern Cuba (Figure 10), which were metamorphosed during subduction onset of the young and hot proto-Caribbean oceanic plate [*Blanco-Quintero et al*., 2010]. However, geochemical data suggest that the protolith of the present samples is probably arc-related mafic igneous rocks, rather than oceanic basalts scraped off from the subducting slab (e.g., MORB) as for the Caribbean rocks. Moreover, no isobaric cooling and blueschist facies overprinting occurred in the present samples as indicated by the absence of glaucophane and phengite in the mineral assemblage. The near-isothermal compression path, however, requires rapid burial along a bent isotherm (~690°C), which is most likely induced by subduction of a cold oceanic slab. We interpret these rocks as part of a continental arc (Figure 11a) that was later transformed to a fore arc close to the subduction channel due to subduction erosion (Figure 11b). Subduction erosion of fore-arc basement rocks, called basal erosion, is an efficient process of crustal recycling into the mantle, resulting in a significant mass loss of older arcs and landward migration of the trench and arc magmatism [e.g., *von Huene and Scholl*, 1991; *Stern*, 2011]. The resultant crustal thickening in the fore-arc region led to burial and heating of previous arc rocks into the lower crust adjacent to the subduction channel, where the isotherms were bent due to cooling by the subducting oceanic slab (Figure 11b). Further burial of these rocks along the bent isotherms resulted in near-isothermal compression until entrained in the subduction channel. Most of these continental arc rocks would have been recycled back into the mantle by subduction erosion and only rarely be able to exhume, probably due to influence of the forced upward flow along the interface of subduction channel and overlying fore-arc basement [*Gerya et al*., 2002]. *Liu et al*. [2014] recently invoked this process to interpret the origin of some HP-UHP rocks with a protolith of magmatic arc affinity in the Southern Tianshan, although no *P-T* path was reported.

Zircon U-Pb dating shows that at least two metamorphic events at ca. 1.9–1.7 Ga and ca. 830–800 Ma, respectively, are recorded in some samples. We suggest that the metamorphic *P-T* path documented above corresponds to the ca. 830–800 Ma metamorphic event, because (1) the ca. 830–800 Ma metamorphic ages are recorded in all samples, whereas the ca. 1.9–1.7 Ga zircons are absent in some samples; (2) the ca. 1.9–1.7 Ga metamorphic zircons, where present, occur as residual cores overgrown by ca. 830–800 Ma rims; (3) the peak metamorphic temperatures are close to the average Ti-in-zircon temperatures for the ca.

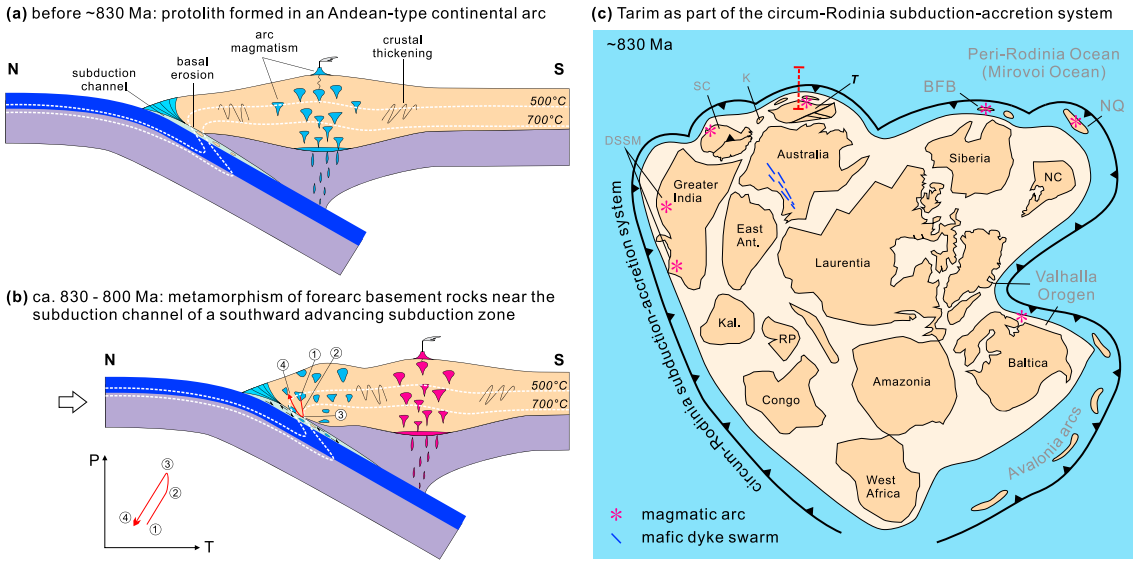

Figure 11. Tectonic and geodynamic model for the formation of the mid-Neoproterozoic high-grade metamorphic rocks in the northern Tarim Craton. (a) Emplacement of the protolith as arc-related mafic igneous rocks in an Andean-type continental arc before ~830 Ma. (b) Southward advance of the subduction zone led to landward migration of the trench and arc magmatism through basal erosion. Previous arc-related rocks were transformed to the fore arc, where they were buried and metamorphosed due to crustal thickening, partly along the bent isotherm at the junction of the fore arc and subduction channel. The retrograde exhumation and cooling were probably triggered by the forced return flow (small arrows) in the subduction channel. The arrow line shows the deduced burial and exhumation path. The inset shows the simplified *P-T* path. The numbers refer to different metamorphic stages. (c) Reconstruction of the Rodinia supercontinent at ~830 Ma, showing Tarim as part of the global-scale circum-Rodinia subduction-accretionary orogenic system. Modified after *Cawood et al.* [2013] and *Ge et al.* [2014a]. Other possible constituents of the circum-Rodinia subduction-accretion system and related arc magmatism at ~830 Ma, as well as the coeval mafic dyke swarms in Australia, are also shown. BFB: Baikalian Fold Belt; DSSM: Delhi Fold Belt-Seychelles-Sri Lanka-Madagascar; K: Kazakhstan blocks; Kal: Kalahari; NC: North China; NQ: Northern Qinling; RP: Rio Plata; SC: South China; T: greater Tarim.

830–800 Ma metamorphic zircons in samples 11K17 (669–689°C) and 12K24 (634–650°C) but lower than those for the ca. 1.9–1.7 Ga zircons (712–773°C); and (4) garnet, clinopyroxene, and titanite inclusions have been found in the ca. 830–800 Ma metamorphic zircons in samples 11K17 and 12K24 but are absent in the 1.9–1.7 Ga zircons (unpublished). Therefore, we suggest that the counterclockwise *P-T* path and the inferred subduction-accretion occurred in the middle Neoproterozoic (~830–800 Ma). The ca. 1.9–1.7 Ga zircons probably record a late Paleoproterozoic tectonothermal event of the surrounding rocks, which has been widely documented in the study area [e.g., *Long et al.*, 2010; *Dong et al.*, 2011; *Zhang et al.*, 2012b; *Ge et al.*, 2013a, 2013b] and were entrained as xenocrysts during magma emplacement.

During which metamorphic stage (prograde, peak, or retrograde) metamorphic zircon forms is important to tie down the *P-T-t* path [e.g., *Harley et al.*, 2007]. The ca. 830–800 Ma metamorphic zircons in the studied samples show steep HREE patterns even for samples 11K17 and 12K24 that contain abundant garnet (Figure 9d). This is different from the relatively flat HREE patterns for metamorphic zircons formed during garnet growth [e.g., *Rubatto and Hermann*, 2007], implying metamorphic zircon growth during the retrograde stage, rather than the prograde or peak stage, because phase diagram modeling shows that the prograde and peak stages are characterized by considerable garnet growth, whereas the retrograde stage is characterized by garnet decomposition. Indeed, the average Ti-in-zircon temperatures for the ca. 830–800 Ma metamorphic zircons in samples 11K17 and 12K24 are slightly lower than the peak metamorphic temperatures obtained above. Moreover, it is noted that some ca. 830–800 Ma metamorphic zircons have very high initial $^{176}Hf/^{177}Hf$ values (0.28227–0.28262), corresponding to positive $\varepsilon_{Hf(t)}$ (+0.2 to +13.0). One interpretation is that the positive $\varepsilon_{Hf(t)}$ could have been inherited from the protolith (i.e., arc-related basalts) that was likely derived from the depleted mantle wedge. This would imply that the protolith was not significantly old relative to the time of metamorphism. Alternatively, the high initial $^{176}Hf/^{177}Hf$ values can be interpreted as new zircon growth/overgrowth incorporating Hf (and Zr) released by garnet decomposition, because garnet has very high $^{176}Lu/^{177}Hf$ ratios [e.g., *Klemd et al.*, 2011] and is able to accumulate considerable radiogenic ^{176}Hf in a relatively short period (Figure 9c). This later interpretation supports the conclusion that the ca. 830–800 Ma metamorphic zircon ages date the early cooling and exhumation event. It is noted that the

metamorphic zircons with different average Ti-in-zircon temperatures yield indistinguishable U-Pb ages within error, implying that the exhumation and cooling occurred in a relative short period (<30 Myr).

7.3. Implications for the Tectonic Evolution of the Tarim Craton and Rodinia

Two contrasting models have been proposed for the Neoproterozoic tectonic evolution of the Tarim Craton: a collision-breakup model [e.g., *Lu et al*., 2008; *Shu et al*., 2011; *Long et al*., 2011; *Zhang et al*., 2012a] and a long-lived subduction-accretion model [*Ge et al*., 2014a]. The former envisages a Grenvillian tectonothermal event in the Tarim Craton as part of the global Rodinia assembly process. However, this is only based on a few imprecise $^{40}Ar/^{39}Ar$, whole-rock Sm-Nd and zircon U-Pb ages of magmatic rocks [*Zhang et al*., 2003, 2012a, 2012b; *Lu et al*., 2008; *Shu et al*., 2011], and there is little metamorphic or structural evidence for such a latest Mesoproterozoic to early Neoproterozoic collisional orogeny in the Tarim Craton. This model also interprets the subsequent middle to late Neoproterozoic (ca. 830–600 Ma) diverse magmatic rocks and sedimentary basins as a response to continental rifting due to multiple episodes of mantle plume activity during the breakup of Rodinia [e.g., *Lu et al*., 2008; *Xu et al*., 2009; *Long et al*., 2011; *Shu et al*., 2011; *Zhang et al*., 2012a]. However, no definitive evidence for a mantle plume (e.g., komatiite, continental flood basalt, radiating mafic dyke swarm) has been found. Especially, the magmatic rocks are dominated by ca. 830–780 Ma calc-alkaline granitoids derived from reworking of ancient, anhydrous, and thickened continental lower crust, possibly due to influx of fluids [*Ge et al*., 2014a] rather than heat [*Long et al*., 2011]. Moreover, minor mafic and ultramafic rocks are nearly all characterized by arc-like geochemical signatures (e.g., depletions of Nb-Ta-Ti and locally Zr-Hf). *Zhang et al*. [2012a] proposed a mantle plume-plate subduction interaction model to reconcile the discrepancy with the mantle plume model, but these authors precluded oceanic subduction after ca. 760 Ma. In contrast, *Ge et al*. [2014c] recently proposed a Neoproterozoic to Paleozoic (950–300 Ma) long-lived subduction-accretionary orogen model for the greater Tarim Craton that includes the Yili-Central Tianshan blocks to the north and the Quanji-Qilian-Alxa blocks to the south. This model interprets the early Neoproterozoic (950–900 Ma) gneissic granitoids in the Yili-Central Tianshan blocks and the middle Neoproterozoic (830–780 Ma) granitoids in the Kuruktag Block as a result of southward migration of arc magmatism due to advancing-type subduction-accretion (Figure 11b), whereas the middle to late Neoproterozoic (780–600 Ma) mafic dyke swarms, A2-type granites, bimodal intrusive complexes and volcanic rocks, and tillite-bearing rift basins were interpreted as a result of retreating-type subduction-accretion and back-arc rifting due to slab rollback. The latter process probably led to separation of the Yili-Central Tianshan continental arcs and back-opening of the Southern Tianshan Ocean, which was subsequently closed by divergent double subduction during the middle to late Paleozoic, docking Tarim to the CAOB [*Ge et al*., 2014a].

The ca. 830–800 Ma high-grade metamorphic rocks documented above, together with the ca. 820–790 Ma mafic and felsic granulites [*He et al*., 2012] and the ca. 830–800 Ma leucogranites [*Ge et al*., 2013b], provide robust evidence for middle Neoproterozoic high-grade regional metamorphism in the Kuruktag Block and suggest that the Tarimian Orogeny is not Grenvillian in age as envisaged [e.g., *Lu et al*., 2008; *Shu et al*., 2011; *Zhang et al*., 2012a; *Kröner et al*., 2013a] but middle Neoproterozoic as originally deduced by *Lu* [1992]. Moreover, the geochemical data and the counterclockwise *P-T* path presented above are consistent with a southward advancing-type subduction-accretion during 830–800 Ma. The ~750–700 Ma blueschists and related metamorphic rocks in the Aksu area [*Liou et al*., 1989, 1996; *Nakajima et al*., 1990; *Zhang et al*., 1999; *Zhu et al*., 2011a; *Yong et al*., 2012] also strongly support the long-lived subduction-accretion model for the northern Tarim Craton [*Ge et al*., 2014a]. As the 830–700 Ma interval is coincident with the time of initial rifting in the interior of Rodinia [e.g., *Li et al*., 2008], the presence of this long-lived Neoproterozoic subduction-accretionary orogeny system provides an independent tectonic constraint for the peripheral position of the Tarim Craton in the Rodinia reconstruction. This is consistent with recent paleomagnetic constraints from the Neoproterozoic strata and mafic dykes in Tarim [e.g., *Chen et al*., 2004; *Wen et al*., 2013; *Zhao et al*., 2014]. We conclude that the long-lived Neoproterozoic subduction-accretionary orogeny in the northern Tarim Craton was most likely a part of the global-scale subduction-accretion system at the peripheral of Rodinia (Figure 11c) [*Cawood et al*., 2013; *Ge et al*., 2014a]. It is noted that the initiation (~950–900 Ma) and southward advance (~830–800 Ma) of this accretionary orogen are synchronous with the final assembly and initial rifting of Rodinia, respectively, suggesting a geodynamic coupling between tectonic processes at the interior and exterior of the supercontinent, possibly related to global plate kinematic adjustment and deep mantle dynamics [e.g., *Cawood and Buchan*, 2007].

The two contrasting models discussed above highlight different tectonic responses of continental blocks located in the interior and at the periphery of a supercontinent during its assembly and breakup. For the core building blocks of Rodinia, like Laurentia and Australia, large-scale collisional orogeny and continental rifting are the main manifestations of supercontinent assembly and breakup, respectively. However, for peripheral blocks facing the Panthalassa-like, Peri-Rodinia (aka Mirovoi) Ocean, no continental collision should be expected at the oceanward margins. Instead, peripheral subduction and accretion probably had a dominant control on the geological evolution and may have been long lasting, perhaps during or after the breakup of Rodinia.

The above generalization also applies for the South China Block. *Li et al*. [1995, 2008] interpreted South China as a "missing link" between Laurentia and Australia in the interior of Rodinia based on the proposed Grenvillian collisional orogens and subsequent mantle plume-induced continental rifting. Alternatively, South China has been interpreted as an exterior subduction-accretionary orogenic system at the periphery of Rodinia based on recognition of prolonged (950–735 Ma) arc magmatism in the western margin and reassignment of a middle Neoproterozoic (~830 Ma) age, rather than Grenvillian, for the Jiangnan Orogen [e.g., *Zhou et al*., 2002; *Cawood et al*., 2013]. If the latter model is correct, South China would have been another important constituent of the circum-Rodinia subduction-accretion system [*Cawood et al*., 2013], probably adjacent to Tarim at the northwestern margin of Rodinia (Figure 11c).

In addition to Tarim and South China, other segments of the circum-Rodinia subduction-accretion system have been documented in a few localities. For example, *Murphy et al*. [2000] suggested that the 1200–660 Ma Avalonia arc magmatism occurred in the Panthalassa-like Peri-Rodinia Ocean along the western Gondwana margin of Rodinia (Figure 11c) and were linked to the amalgamation and dispersal in the interior. *Cawood et al*. [2010] proposed that the ca. 1030–710 Ma Valhalla orogen in North Atlantic was also an accretionary orogen along the Laurentia and Baltic margin of Rodinia (Figure 11c) that initiated synchronously with the Grenville-Sveconorwegian Orogen in the interior. The ca. 1100–700 Ma magmatic and deformation events in blocks originally located in the western greater India, including Sri Lanka [e.g., *Kröner et al*., 2003, 2013b], Madagascar [e.g., *Handke et al*., 1999], Seychelles [e.g., *Torsvik et al*., 2001], and the Delhi Fold Belt [e.g., *Dharma Rao et al*., 2013], were also considered by many as formed by subduction-accretion along the western margin of Rodinia. Other possible records of the circum-Rodinia subduction-accretion system include the ca. 1000–620 Ma Baikalian Fold Belt in southern Siberia [e.g., *Rytsk et al*., 2011], the ca. 1300–780 Ma arc-related (?) magmatic rocks in the Kokchetav-North Tianshan belt of Central Asia [e.g., *Kröner et al*., 2013a], and the 1000–840 Ma magmatic rocks and ophiolites in the Northern Qinling Terrane of the North China Craton [*Dong et al*., 2014]. All these tectonic units were possibly located along the periphery of Rodinia (Figure 11c), where widespread tectonothermal activity initiated during the assembly stage and lasted to the breakup stage of the supercontinent and is generally consistent with the establishment of a long-lived circum-Rodinia subduction system. This provides a new clue for the interpretation of the global tectonic setting of these regional events. Particularly, the broad comparability of the long-lived accretionary orogen proposed here in the northern Tarim and the tectonothermal records in the southern Siberia [e.g., *Rytsk et al*., 2011] and the Kokchetav-North Tianshan belt [e.g., *Kröner et al*., 2013a] suggest that the early evolution of the CAOB probably initiated as part of the circum-Rodinia subduction-accretionary system and that the so-called Paleo-Asian Oceanic is not a "static" ocean intervening between Siberia, Baltic, Tarim, and North China but just a remnant of the Panthalassa-like Mirovoi Ocean [*Ge et al*., 2014a]. This provides an innovative and testable model for future studies of the CAOB.

8. Conclusions

The studied metamafic and calc-silicate rocks were probably derived from continental arc magmatic rocks that were significantly altered by Ca-rich fluids. They experienced ca. 830–800 Ma upper amphibolite to high-pressure granulite facies metamorphism along a counterclockwise *P-T* path involving near-isothermal burial. The apparent geothermal gradient (~18°C km^{-1}) deduced from peak metamorphic temperature and pressure is consistent with intermediate d*T*/d*P* type metamorphism in subduction-to-collision orogenic settings. The counterclockwise *P-T* path is similar to those recorded in some high-grade rocks in subduction mélanges formed during subduction initiation of young and hot oceanic plates. However, considering their continental origin, the present samples were interpreted to have been metamorphosed during crustal

thickening when they were transformed from arc to fore arc by subduction erosion due to advance of a subducting oceanic slab. The near-isothermal compression path probably records burial along the bent isotherm near the subduction channel, whereas the final cooling and exhumation was probably triggered by the forced upward return flow along the interface of the fore-arc basement and the subduction channel. This study thus provides metamorphic evidence for a mid-Neoproterozoic advancing-type accretionary orogeny (the Tarimian Orogeny) in the northern Tarim Craton. As this accretionary orogenic event occurred during the initial stage of Rodinia breakup, it provides an independent tectonic constraint for a peripheral position for the Tarim Craton in the Rodinia reconstruction. It is also reasonable to conclude that this mid-Neoproterozoic accretionary orogeny was a part of the global-scale circum-Rodinia subduction-accretion system, which is probably also recorded in many other localities worldwide and is therefore important for our understanding of the evolution of the Rodinia supercontinent.

Acknowledgments

We thank P.J. Lin, F.C. Li, B. Wu, M.Q. Zhang, and T. Yang for kind assistance with the laboratory analyses, and Z.Y. He and Z.L. Tian for discussions on metamorphic petrology and phase diagram modeling. Comments by P.A. Cawood and P. Agard on an early version of this manuscript and review by W. J. Collin and an anonymous reviewer significantly improved this paper. Editorial handling by Claudio Faccenna and Karel Schulmann is also appreciated. This research was financially supported by grants from the National the Natural Science Foundation of China (41502178 and 41272211), the Natural Science Foundation of Jiangsu Province (BK20150577), the State Key Laboratory for Mineral Deposits Research of Nanjing University (ZZKT-201603), and the China Postdoctoral Science Foundation (2015 M570432). All analytical results are presented in supporting information, and the original data are available upon request from the first author.

References

Auzanneau, E., M. W. Schmidt, D. Vielzeuf, and J. D. Connolly (2010), Titanium in phengite: A geobarometer for high temperature eclogites, *Contrib. Mineral. Petrol.*, *159*, 1–24, doi:10.1007/s00410-009-0412-7.

Beinlich, A., R. Klemd, T. John, and J. Gao (2010), Trace-element mobilization during Ca-metasomatism along a major fluid conduit: Eclogitization of blueschist as a consequence of fluid-rock interaction, *Geochim. Cosmochim. Acta*, *74*, 1892–1922, doi:10.1016/j.gca.2009.12.011.

Berman, R. G., L. Y. Aranovich, and D. Pattison (1995), Reassessment of the garnet-clinopyroxene Fe–Mg exchange thermometer: II. Thermodynamic analysis, *Contrib. Mineral. Petrol.*, *119*, 30–42, doi:10.1007/BF00310715.

Bhowmik, S. K., and A. Ao (2016), Subduction initiation in the Neo-Tethys: Constraints from counterclockwise *P-T* paths in amphibolite rocks of the Nagaland Ophiolite Complex, India, *J. Metamorph. Geol.*, *34*, 17–44, doi:10.1111/jmg.12169.

Blanco-Quintero, I. F., A. García-Casco, Y. Rojas-Agramonte, A. Rodríguez-Vega, C. Lázaro, and M. A. Iturralde-Vinent (2010), Metamorphic evolution of subducted hot oceanic crust (La Corea Mélange, Cuba), *Am. J. Sci.*, *310*, 889–915, doi:10.2475/11.2010.01.

Brown, M. (2007), Metamorphic conditions in orogenic belts: A record of secular change, *Int. Geol. Rev.*, *49*, 193–234, doi:10.2747/0020-6814.49.3.193.

Brown, M. (2009), *Metamorphic Patterns in Orogenic Systems and the Geological Record*, vol. 318, pp. 37–74, Geol. Soc., London Spec. Publ., doi:10.1144/SP318.2.

Brown, M. (2014), The contribution of metamorphic petrology to understanding lithosphere evolution and geodynamics, *Geosci. Front.*, *5*, 553–569.

Cawood, P. A. (2005), Terra Australis Orogen: Rodinia breakup and development of the Pacific and Iapetus margins of Gondwana during the Neoproterozoic and Paleozoic, *Earth Sci. Rev.*, *69*, 249–279, doi:10.1016/j.earscirev.2004.09.001.

Cawood, P. A., and C. Buchan (2007), Linking accretionary orogenesis with supercontinent assembly, *Earth Sci. Rev.*, *82*, 217–256, doi:10.1016/j.earscirev.2007.03.003.

Cawood, P. A., R. Strachan, K. Cutts, P. D. Kinny, M. Hand, and S. Pisarevsky (2010), Neoproterozoic orogeny along the margin of Rodinia: Valhalla orogen, North Atlantic, *Geology*, *38*, 99–102, doi:10.1130/G30450.1.

Cawood, P. A., Y. J. Wang, Y. J. Xu, and G. C. Zhao (2013), Locating South China in Rodinia and Gondwana: A fragment of greater India lithosphere?, *Geology*, *8*, 903–906, doi:10.1130/G34395.1.

Chen, Y., B. Xu, S. Zhan, and Y. G. Li (2004), First mid-Neoproterozoic Paleomagnetic results from the Tarim Basin (NW China) and their geodynamic implications, *Precambrian Res.*, *133*, 271–281, doi:10.1016/j.precamres.2004.05.002.

Connolly, J. A. D. (2005), Computation of phase equilibria by linear programming: A tool for geodynamic modeling and its application to subduction zone decarbonation, *Earth Planet. Sci. Lett.*, *236*, 524–541, doi:10.1016/j.epsl.2005.04.033.

Dalziel, I. W. D. (1991), Pacific margins of Laurentia and East Antarctica-Australia as a conjugate rift pair: Evidence and implications for an Eocambrian supercontinent, *Geology*, *19*, 598–601, doi:10.1130/0091-7613(1991)019<0598:PMOLAE>2.3.CO;2.

Dharma Rao, C. V., M. Santosh, S. W. Kim, and S. Li (2013), Arc magmatism in the Delhi Fold Belt: SHRIMP U-Pb zircon ages of granitoids and implications for Neoproterozoic convergent margin tectonics in NW India, *J. Asian Earth Sci.*, *78*, 83–99, doi:10.1016/j.jseaes.2012.09.007.

Diener, J. F. A., and R. Powell (2012), Revised activity-composition models for clinopyroxene and amphibole, *J. Metamorph. Geol.*, *30*, 131–142, doi:10.1111/j.1525-1314.2011.00959.x.

Dong, X., Z. M. Zhang, and W. Tang (2011), Precambrian tectono-thermal events of the northern margin of the Tarim Craton: Constraints of zircon U-Pb chronology from high-grade metamorphic rocks of the Korla, *Acta Petrol. Sin.*, *27*, 47–58.

Dong, Y., Z. Yang, X. Liu, X. Zhang, D. He, W. Li, F. Zhang, S. Sun, H. Zhang, and G. Zhang (2014), Neoproterozoic amalgamation of the Northern Qinling terrain to the North China Craton: Constraints from geochronology and geochemistry of the Kuanping ophiolite, *Precambrian Res.*, *255*, 77–95, doi:10.1016/j.precamres.2014.09.008.

Evans, D. A. D. (2009), *The Palaeomagnetically Viable, Long-Lived and All-Inclusive Rodinia Supercontinent Reconstruction*, Geol. Soc. London Spec. Publ., *327*, 371–404, doi:10.1144/SP327.16.

Evans, D. A. D. (2013), Reconstructing pre-Pangean supercontinents, *Geol. Soc. Am. Bull.*, *125*, 1735–1751, doi:10.1130/B30950.1.

Ferry, J., and E. Watson (2007), New thermodynamic models and revised calibrations for the Ti-in-zircon and Zr-in-rutile thermometers, *Contrib. Mineral. Petrol.*, *154*, 429–437, doi:10.1007/s00410-007-0201-0.

Ferry, J. M., and J. G. Blencoe (1978), Subsolidus phase relations in the nepheline-kalsilite system at 0.5, 2.0, and 5.0 kbar, *Am. Mineral.*, *63*, 1225–1240.

Fuhrman, M. L., and D. H. Lindsley (1988), Ternary-feldspar modeling and thermometry, *Am. Mineral.*, *73*, 201–215.

Ganguly, J., W. Cheng, and M. Tirone (1996), Thermodynamics of aluminosilicate garnet solid solution: New experimental data, an optimized model, and thermometric applications, *Contrib. Mineral. Petrol.*, *126*, 137–151, doi:10.1007/s004100050240.

Gao, J., X. Wang, R. Klemd, T. Jiang, Q. Qian, L. Mu, and Y. Ma (2015), Record of assembly and breakup of Rodinia in the Southwestern Altaids: Evidence from Neoproterozoic magmatism in the Chinese Western Tianshan Orogen, *J. Asian Earth Sci.*, doi:10.1016/j.jseaes.2015.02.002.

Gao, Z. J., J. B. Chen, S. N. Lu, C. W. Peng, and Z. Y. Qin (1993), *The Precambrian Geology in Northern Xinjiang (Precambrian Geology No. 6)*, Geol. House, Beijing.

Ge, R. F., W. B. Zhu, B. H. Zheng, H. L. Wu, J. W. He, and X. Q. Zhu (2012a), Early Pan-African magmatism in the Tarim Craton: Insights from zircon U-Pb-Lu-Hf isotope and geochemistry of granitoids in the Korla area, NW China, *Precambrian Res.*, *212–213*, 117–138, doi:10.1016/j.precamres.2012.05.001.

Ge, R. F., W. B. Zhu, H. L. Wu, B. H. Zheng, X. Q. Zhu, and J. W. He (2012b), The Paleozoic northern margin of the Tarim Craton: Passive or active?, *Lithos*, *142–143*, 1–15, doi:10.1016/j.lithos.2012.02.010.

Ge, R. F., W. B. Zhu, H. L. Wu, J. W. He, and B. H. Zheng (2013a), Zircon U-Pb ages and Lu-Hf isotopes of Paleoproterozoic metasedimentary rocks in the Korla Complex, NW China: Implications for metamorphic zircon formation and geological evolution of the Tarim Craton, *Precambrian Res.*, *231*, 1–18, doi:10.1016/j.precamres.2013.03.003.

Ge, R. F., W. B. Zhu, H. L. Wu, B. H. Zheng, and J. W. He (2013b), Timing and mechanisms of multiple episodes of migmatization in the Korla Complex, northern Tarim Craton, NW China: Constraints from zircon U-Pb-Lu-Hf isotopes and implications for crustal growth, *Precambrian Res.*, *231*, 136–156, doi:10.1016/j.precamres.2013.03.005.

Ge, R. F., W. B. Zhu, S. A. Wilde, J. W. He, X. Cui, X. Wang, and B. Zheng (2014a), Neoproterozoic to Paleozoic long-lived accretionary orogeny in the northern Tarim Craton, *Tectonics*, *33*, 302–329, doi:10.1002/2013TC003501.

Ge, R. F., W. B. Zhu, S. A. Wilde, H. L. Wu, J. W. He, and B. H. Zheng (2014b), Archean magmatism and crustal evolution in the northern Tarim Craton: Insights from zircon U-Pb-Hf-O isotopes and geochemistry of ~2.7 Ga orthogneiss and amphibolite in the Korla Complex, *Precambrian Res.*, *252*, 145–165, doi:10.1016/j.precamres.2014.07.019.

Ge, R. F., W. B. Zhu, S. A. Wilde, and J. W. He (2014c), Zircon U-Pb-Lu-Hf-O isotopic evidence for ≥3.5 Ga crustal growth, reworking and differentiation in the northern Tarim Craton, *Precambrian Res.*, *249*, 115–128, doi:10.1016/j.precamres.2014.05.004.

Ge, R. F., W. B. Zhu, S. A. Wilde, J. W. He, and X. Cui (2015), Synchronous crustal growth and reworking recorded in late Paleoproterozoic granitoids in the northern Tarim Craton: In situ zircon U-Pb-Hf-O isotopic and geochemical constraints and tectonic implications, *Geol. Soc. Am. Bull.*, *127*, 781–803, doi:10.1130/B31050.1.

Gehrels, G. E., A. Yin, and X. Wang (2003), Magmatic history of the northeastern Tibetan Plateau, *J. Geophys. Res.*, *108*(B9), 2423, doi:10.1029/2002JB001876.

Gerdes, A., and A. Zeh (2009), Zircon formation versus zircon alteration—New insights from combined U-Pb and Lu-Hf in-situ LA-ICP-MS analyses, and consequences for the interpretation of Archean zircon from the Central Zone of the Limpopo Belt, *Chem. Geol.*, *261*, 230–243, doi:10.1016/j.chemgeo.2008.03.005.

Gerya, T. V., B. Stöckhert, and A. L. Perchuk (2002), Exhumation of high-pressure metamorphic rocks in a subduction channel: A numerical simulation, *Tectonics*, *21*(6), 1056, doi:10.1029/2002TC001406.

Guo, R. Q., A. Nijiati, Q. Qin, X. L. Jia, Z. X. Zhu, K. Z. Wang, and Y. P. Li (2013), Geological characteristics and tectonic significance of Silurian granitic intrusions in the northern Tarim Craton, Xinjiang, *Geol. Bull. China*, *32*, 220–238.

Handke, M. J., R. D. Tucker, and L. D. Ashwal (1999), Neoproterozoic continental arc magmatism in west-central Madagascar, *Geology*, *27*, 351–354, doi:10.1130/0091-7613(1999)027<0351:NCAMIW>2.3.CO;2.

Harley, S. L., N. M. Kelly, and A. Moller (2007), Zircon behaviour and the thermal histories of mountain chains, *Elements*, *3*, 25–30, doi:10.2113/gselements.3.1.25.

He, J. W., W. B. Zhu, and R. F. Ge (2014a), New age constraints on Neoproterozoic diamicites in Kuruktag, NW China and Precambrian crustal evolution of the Tarim Craton, *Precambrian Res.*, *241*, 44–60, doi:10.1016/j.precamres.2013.11.005.

He, J. W., W. B. Zhu, R. F. Ge, B. H. Zheng, and H. L. Wu (2014b), Detrital zircon U-Pb ages and Hf isotopes of Neoproterozoic strata in the Aksu area, northwestern Tarim Craton: Implications for supercontinent reconstruction and crustal evolution, *Precambrian Res.*, *254*, 194–209, doi:10.1016/j.precamres.2014.08.016.

He, Z. Y., Z. M. Zhang, K. Q. Zong, W. Wang, and M. Santosh (2012), Neoproterozoic granulites from the northeastern margin of the Tarim Craton: Petrology, zircon U-Pb ages and implications for the Rodinia assembly, *Precambrian Res.*, *212-213*, 21–33, doi:10.1016/j.precamres.2012.04.014.

He, Z. Y., Z. M. Zhang, K. Q. Zong, and X. Dong (2013), Paleoproterozoic crustal evolution of the Tarim Craton: Constrained by zircon U-Pb and Hf isotopes of meta-igneous rocks from Korla and Dunhuang, *J. Asian Earth Sci.*, *78*, 54–70, doi:10.1016/j.jseaes.2013.07.022.

Hoffman, P. F. (1991), Did the breakout of Laurentia turn Gondwanaland inside-out?, *Science*, *252*, 1409–1412, doi:10.1126/science.252.5011.1409.

Holland, T. J. B., and R. Powell (1998), An internally consistent thermodynamic data set for phases of petrological interest, *J. Metamorph. Geol.*, *16*, 309–343, doi:10.1111/j.1525-1314.1998.00140.x.

Huang, B. T., Z. Y. He, K. Q. Zong, and Z. M. Zhang (2014), Zircon U-Pb and Hf isotopic study of Neoproterozoic granitic gneisses from the Alatage area, Xinjiang: Constraints on the Precambrian crustal evolution in the Central Tianshan Block, *Chinese Sci. Bull.*, *59*, 100–112, doi:10.1007/s11434-013-0010-y.

John, T., R. Klemd, J. Gao, and C. Garbe-Schönberg (2008), Trace-element mobilization in slabs due to non steady-state fluid-rock interaction: Constraints from an eclogite-facies transport vein in blueschist (Tianshan, China), *Lithos*, *103*, 1–24, doi:10.1016/j.lithos.2007.09.005.

Klemd, R. (2013), Metasomatism during high-pressure metamorphism: Eclogites and blueschist-facies rocks, in *Metasomatism and the Chemical Transformation of Rock*, edited by D. E. Harlov and H. Austrheim, pp. 351–413, Springer, Heidelberg.

Klemd, R., T. John, E. E. Scherer, S. Rondenay, and J. Gao (2011), Changes in dip of subducted slabs at depth: Petrological and geochronological evidence from HP-UHP rocks (Tianshan, NW-China), *Earth Planet. Sci. Lett.*, *310*, 9–20, doi:10.1016/j.epsl.2011.07.022.

Kohn, M. J. (2003), Geochemical zoning in metamorphic minerals, in *Treatise on Geochemistry*, edited by R. L. Rudnick, pp. 249–280, Elsevier, Amsterdam.

Kröner, A., K. V. W. Kehelpannala, and E. Hegner (2003), Ca. 750–1100 Ma magmatic events and Grenville-age deformation in Sri Lanka: Relevance for Rodinia supercontinent formation and dispersal, and Gondwana amalgamation, *J. Asian Earth Sci.*, *22*, 279–300, doi:10.1016/S1367-9120(03)00060-9.

Kröner, A., et al. (2013a), Mesoproterozoic (Grenville-age) terranes in the Kyrgyz North Tianshan: Zircon ages and Nd-Hf isotopic constraints on the origin and evolution of basement blocks in the southern Central Asian Orogen, *Gondwana Res.*, doi:10.1016/j.gr.2012.05.004.

Kröner, A., Y. Rojas-Agramonte, K. V. W. Kehelpannala, T. Zack, E. Hegner, H. Y. Geng, J. Wong, and M. Barth (2013b), Age, Nd-Hf isotopes, and geochemistry of the Vijayan Complex of eastern and southern Sri Lanka: A Grenville-age magmatic arc of unknown derivation, *Precambrian Res.*, *234*, 288–321, doi:10.1016/j.precamres.2012.11.001.

Leake, B. E. (1964), The chemical distinction between ortho- and para-amphibolites, *J. Petrol.*, *5*, 238–254, doi:10.1093/petrology/5.2.238.

Li, Z. X., and S. J. Zhong (2009), Supercontinent-superplume coupling, true polar wander and plume mobility: Plate dominance in whole-mantle tectonics, *Phys. Earth Planet. Inter.*, *176*, 143–156, doi:10.1016/j.pepi.2009.05.004.

Li, Z. X., L. H. Zhang, and C. M. Powell (1995), South China in Rodinia—Part of the missing link between Australia-East Antarctica and Laurentia, *Geology*, *23*, 407–410, doi:10.1130/0091-7613(1995)023<0407:SCIRPO>2.3.CO;2.

Li, Z. X., L. Zhang, and C. M. Powell (1996), Positions of the East Asian Cratons in the Neoproterozoic supercontinent Rodinia, *Aust. J. Earth Sci.*, *43*, 593–604, doi:10.1080/08120099608728281.
Li, Z. X., et al. (2008), Assembly, configuration, and break-up history of Rodinia: A synthesis, *Precambrian Res.*, *160*, 179–210, doi:10.1016/j.precamres.2007.04.021.
Liou, J. G., et al. (1989), Proterozoic blueschist belt in western China: Best documented Precambrian blueschists in the world, *Geology*, *17*, 1127–1131, doi:10.1130/0091-7613(1989)017<1127:PBBIWC>2.3.CO;2.
Liou, J. G., S. A. Graham, S. Maruyama, and R. Y. Zhang (1996), Characteristics and tectonic significance of the Late Proterozoic Aksu blueschists and diabasic dikes, northwest Xinjiang, China, *Int. Geol. Rev.*, *38*, 228–244, doi:10.1080/00206819709465332.
Liu, X., W. Su, J. Gao, J. Li, T. Jiang, X. Zhang, and X. Ge (2014), Paleozoic subduction erosion involving accretionary wedge sediments in the South Tianshan Orogen: Evidence from geochronological and geochemical studies on eclogites and their host metasediments, *Lithos*, *210–211*, 89–110, doi:10.1016/j.lithos.2014.09.017.
Long, X. P., C. Yuan, M. Sun, G. C. Zhao, W. J. Xiao, Y. J. Wang, Y. H. Yang, and A. Q. Hu (2010), Archean crustal evolution of the northern Tarim Craton, NW China: Zircon U-Pb and Hf isotopic constraints, *Precambrian Res.*, *180*, 272–284, doi:10.1016/j.precamres.2010.05.001.
Long, X. P., C. Yuan, M. Sun, A. Kröner, G. C. Zhao, S. Wilde, and A. Q. Hu (2011), Reworking of the Tarim Craton by underplating of mantle plume-derived magmas: Evidence from Neoproterozoic granitoids in the Kuluketage area, NW China, *Precambrian Res.*, *187*, 1–14, doi:10.1016/j.precamres.2011.02.001.
Long, X., C. Yuan, M. Sun, A. Kröner, and G. Zhao (2014), New geochemical and combined zircon U-Pb and Lu-Hf isotopic data of orthogneisses in the northern Altyn Tagh, northern margin of the Tibetan plateau: Implication for Archean evolution of the Dunhuang Block and crust formation in NW China, *Lithos*, *200–201*, 418–431, doi:10.1016/j.lithos.2014.05.008.
Lu, S. N. (1992), Geological evolution of Proterozoic in Kuruktage, Xinjiang, *Bull. Tianjin Inst. Geol. Mineral Res.*, *26-27*, 279–292.
Lu, S. N., H. K. Li, C. L. Zhang, and G. H. Niu (2008), Geological and geochronological evidence for the Precambrian evolution of the Tarim Craton and surrounding continental fragments, *Precambrian Res.*, *160*, 94–107, doi:10.1016/j.precamres.2007.04.025.
Moores, E. M. (1991), Southwest U.S.-East Antarctic (SWEAT) connection: A hypothesis, *Geology*, *19*, 425–428, doi:10.1130/0091-7613(1991)019<0425:SUSEAS>2.3.CO;2.
Murphy, J. B., and R. D. Nance (1991), Supercontinent model for the contrasting character of Late Proterozoic orogenic belts, *Geology*, *19*, 469–472, doi:10.1130/0091-7613(1991)019<0469:SMFTCC>2.3.CO;2.
Murphy, J. B., R. A. Strachan, R. D. Nance, K. D. Parker, and M. B. Fowler (2000), Proto-Avalonia: A 1.2–1.0 Ga tectonothermal event and constraints for the evolution of Rodinia, *Geology*, *28*, 1071–1074.
Nakajima, T., S. Maruyama, S. Uchiumi, J. G. Liou, X. Wang, X. Xiao, and S. A. Graham (1990), Evidence for late Proterozoic subduction from 700-Myr-old blueschists in China, *Nature*, *346*, 263–265, doi:10.1038/346263a0.
Pearce, J. A. (1996), A user's guide to basalt discrimination diagrams, in *Trace Element Geochemistry of Volcanic Rocks: Applications for Massive Sulphide Exploration*, *Short Course Notes*, vol. 12, pp. 113, Geol. Assoc. of Canada, St. John's.
Pearce, J. A. (2008), Geochemical fingerprinting of oceanic basalts with applications to ophiolite classification and the search for Archean oceanic crust, *Lithos*, *100*, 14–48, doi:10.1016/j.lithos.2007.06.016.
Powell, R., and T. Holland (1994), Optimal geothermometry and geobarometry, *Am. Mineral.*, *79*, 120–133.
Rivers, T. (1997), Lithotectonic elements of the Grenville Province: Review and tectonic implications, *Precambrian Res.*, *86*, 117–154.
Rubatto, D., and J. Hermann (2007), Zircon behaviour in deeply subducted rocks, *Electron. J. Severe Storms Meteorol.*, *3*, 31–35, doi:10.2113/gselements.3.1.31.
Rytsk, E. Y., V. P. Kovach, V. V. Yarmolyuk, V. I. Kovalenko, E. S. Bogomolov, and A. B. Kotov (2011), Isotopic structure and evolution of the continental crust in the East Transbaikalian segment of the Central Asian Foldbelt, *Geotectonics*, *45*, 349–377, doi:10.1134/S0016852111050037.
Shu, L. S., X. L. Deng, W. B. Zhu, D. S. Ma, and W. J. Xiao (2011), Precambrian tectonic evolution of the Tarim Block, NW China: New geochronological insights from the Quruqtagh domain, *J. Asian Earth Sci.*, *42*, 774–790, doi:10.1016/j.jseaes.2010.08.018.
Song, S. G., L. Su, X. H. Li, Y. L. Niu, and L. F. Zhang (2012), Grenville-age orogenesis in the Qaidam-Qilian block: The link between South China and Tarim, *Precambrian Res.*, *220–221*, 9–22, doi:10.1016/j.precamres.2012.07.007.
Stern, C. R. (2011), Subduction erosion: Rates, mechanisms, and its role in arc magmatism and the evolution of the continental crust and mantle, *Gondwana Res.*, *20*, 284–308, doi:10.1016/j.gr.2011.03.006.
Sun, S. S., and W. F. McDonough (1989), *Chemical and Isotopic Systematics of Oceanic Basalts: Implications for Mantle Composition and Processes*, vol. 42, Spec. Pub., pp. 313–345, Geol Soc., London, doi:10.1144/GSL.SP.1989.042.01.19.
Tajčmanová, L., J. Connolly, and B. Cesare (2009), A thermodynamic model for titanium and ferric iron solution in biotite, *J. Metamorph. Geol.*, *27*, 153–165, doi:10.1111/j.1525-1314.2009.00812.x.
Taylor, S. R., and S. M. Mclennan (1985), *The Continental Crust: Its Composition and Evolution*, Blackwell Sci. Publ., Oxford.
Torsvik, T. H., L. D. Ashwal, R. D. Tucker, and E. A. Eide (2001), Neoproterozoic geochronology and palaeogeography of the Seychelles microcontinent: The India link, *Precambrian Res.*, *110*, 47–59, doi:10.1016/S0301-9268(01)00180-2.
von Huene, R., and D. W. Scholl (1991), Observations at convergent margins concerning sediment subduction, subduction erosion, and the growth of continental crust, *Rev. Geophys.*, *29*, 279–316, doi:10.1029/91RG00969.
Waldbaum, D. R., and J. B. Thompson (1968), Mixing properties of sanidine crystalline solutions. 2. Calculations based on volume data, *Am. Mineral.*, *53*, 2000–2017.
Walker, K. R., G. A. Joplin, J. F. Lovering, and R. Green (1959), Metamorphic and metasomatic convergence of basic igneous rocks and lime-magnesia sediments of the Precambrian of North-western Queensland, *J. Geol. Soc. Aust.*, *6*, 149–177, doi:10.1080/00167615908728504.
Wang, C., L. Liu, W. Yang, X. Zhu, Y. Cao, L. Kang, S. Chen, R. Li, and S. He (2013), Provenance and ages of the Altyn Complex in Altyn Tagh: Implications for the early Neoproterozoic evolution of northwestern China, *Precambrian Res.*, *230*, 193–208, doi:10.1016/j.precamres.2013.02.003.
Watson, E., D. Wark, and J. Thomas (2006), Crystallization thermometers for zircon and rutile, *Contrib. Mineral. Petrol.*, *151*, 413–433, doi:10.1007/s00410-006-0068-5.
Wen, B., Y. X. Li, and W. B. Zhu (2013), Paleomagnetism of the Neoproterozoic diamictites of the Qiaoenbrak formation in the Aksu area, NW China: Constraints on the paleogeographic position of the Tarim Block, *Precambrian Res.*, *226*, 75–90, doi:10.1016/j.precamres.2012.10.018.
Wen, B., D. A. D. Evans, Y. Li, Z. Wang, and C. Liu (2015), Newly discovered Neoproterozoic diamictite and cap carbonate (DCC) couplet in Tarim Craton, NW China: Stratigraphy, geochemistry, and paleoenvironment, *Precambrian Res.*, *271*, 278–294, doi:10.1016/j.precamres.2015.10.006.
White, R. W., R. Powell, and T. J. B. Holland (2007), Progress relating to calculation of partial melting equilibria for metapelites, *J. Metamorph. Geol.*, *25*, 511–527, doi:10.1111/j.1525-1314.2007.00711.x.

Whitney, D. L., and B. W. Evans (2010), Abbreviations for names of rock-forming minerals, *Am. Mineral.*, *95*, 185–187.
XBGMR (1959), *1:200000 Geological Map of RPC, Korla Sheet (K-45-XXI)*, Natl. 543 House, Beijing.
XBGMR (1993), *Regional Geology of Xinjiang Uygur Autonomy Region*, Geol. House, Beijing.
Xu, B., S. H. Xiao, H. B. Zou, Y. Chen, Z. X. Li, B. Song, D. Y. Liu, C. M. Zhou, and X. L. Yuan (2009), SHRIMP zircon U-Pb age constraints on Neoproterozoic Quruqtagh diamictites in NW China, *Precambrian Res.*, *168*, 247–258, doi:10.1016/j.precamres.2008.10.008.
Xu, B., H. Zou, Y. Chen, J. He, and Y. Wang (2013), The Sugetbrak basalts from northwestern Tarim Block of northwest China: Geochronology, geochemistry and implications for Rodinia breakup and ice age in the Late Neoproterozoic, *Precambrian Res.*, *236*, 214–226, doi:10.1016/j.precamres.2013.07.009.
Yong, W. J., L. F. Zhang, C. M. Hall, S. B. Mukasa, and E. J. Essene (2012), The $^{40}Ar/^{39}Ar$ and Rb-Sr chronology of the Precambrian Aksu blueschists in western China, *J. Asian Earth Sci.*, *63*, 197–205, doi:10.1016/j.jseaes.2012.05.024.
Yu, S. Y., J. X. Zhang, P. G. Del Real, X. L. Zhao, K. J. Hou, J. H. Gong, and Y. S. Li (2013), The Grenvillian orogeny in the Altun-Qilian-North Qaidam mountain belts of northern Tibet Plateau: Constraints from geochemical and zircon U-Pb age and Hf isotopic study of magmatic rocks, *J. Asian Earth Sci.*, *73*, 372–395, doi:10.1016/j.jseaes.2013.04.042.
Yuan, Y., K. Zong, Z. He, R. Klemd, Y. Liu, Z. Hu, J. Guo, and Z. Zhang (2015), Geochemical and geochronological evidence for a former early Neoproterozoic microcontinent in the South Beishan Orogenic Belt, southernmost Central Asian Orogenic Belt, *Precambrian Res.*, *266*, 409–424, doi:10.1016/j.precamres.2015.05.034.
Zhang, C. L., Y. Zhao, K. Y. Guo, and A. G. Wang (2003), Grenvilie orogeny in north of the Qinghaitibet Plateau: First evidence from isotopic dating, *Sci. Geol. Sin.*, *38*, 535–538.
Zhang, C. L., H. B. Zou, H. Y. Wang, H. K. Li, and H. M. Ye (2012a), Multiple phases of the Neoproterozoic igneous activity in Quruqtagh of the northeastern Tarim Block, NW China: Interaction between plate subduction and mantle plume? *Precambrian Res.*, *222–223*, 488–502, doi:10.1016/j.precamres.2011.08.005.
Zhang, C. L., H. K. Li, M. Santosh, Z. X. Li, H. B. Zou, H. Y. Wang, and H. M. Ye (2012b), Precambrian evolution and cratonization of the Tarim Block, NW China: Petrology, geochemistry, Nd-isotopes and U-Pb zircon geochronology from Archaean gabbro-TTG-potassic granite suite and Paleoproterozoic metamorphic belt, *J. Asian Earth Sci.*, *47*, 5–20, doi:10.1016/j.jseaes.2011.05.018.
Zhang, C. L., H. Zou, M. Santosh, X. Ye, and H. Li (2014), Is the Precambrian basement of the Tarim Craton in NW China composed of discrete terranes?, *Precambrian Res.*, *254*, 226–244, doi:10.1016/j.precamres.2014.08.006.
Zhang, J. X., J. H. Gong, and S. Y. Yu (2012c), c. 1.85 Ga HP granulite-facies metamorphism in the Dunhuang block of the Tarim Craton, NW China: Evidence from U-Pb zircon dating of mafic granulites, *J. Geol. Soc. London*, *169*, 511–514, doi:10.1144/0016-76492011-158.
Zhang, J. X., S. Y. Yu, J. H. Gong, H. K. Li, and K. J. Hou (2013), The latest Neoarchean-Paleoproterozoic evolution of the Dunhuang block, eastern Tarim Craton, northwestern China: Evidence from zircon U-Pb dating and Hf isotopic analyses, *Precambrian Res.*, *226*, 21–42, doi:10.1016/j.precamres.2012.11.014.
Zhang, L., W. Jiang, C. Wei, and S. Dong (1999), Discovery of deerite from the Aksu Precambrian blueschist terrane and its geological significance, *Sci. China Ser. D. Earth Sci.*, *42*, 233–239.
Zhao, G. C., M. Sun, S. A. Wilde, and S. Z. Li (2004), A Paleo-Mesoproterozoic supercontinent: Assembly, growth and breakup, *Earth Sci. Rev.*, *67*, 91–123, doi:10.1016/j.earscirev.2004.02.003.
Zhao, P., Y. Chen, S. Zhan, B. Xu, and M. Faure (2014), The Apparent Polar Wander Path of the Tarim block (NW China) since the Neoproterozoic and its implications for a long-term Tarim-Australia connection, *Precambrian Res.*, *242*, 39–57, doi:10.1016/j.precamres.2013.12.009.
Zhao, Y., C. R. Diwu, W. H. Ao, H. L. Wang, T. Zhu, and Y. Sun (2015), Ca. 3.06 Ga granodioritic gneiss in Dunhuang block, *Chinese Sci. Bull.*, *60*, 75–38, doi:10.1360/N972014-00382.
Zhou, M. F., A. K. Kennedy, M. Sun, J. Malpas, and C. M. Lesher (2002), Neoproterozoic arc-related mafic intrusions along the northern margin of South China: Implications for the accretion of Rodinia, *J. Geol.*, *110*, 611–618, doi:10.1086/341762.
Zhu, W. B., Z. Y. Zhang, L. S. Shu, H. F. Lu, J. B. Su, and W. Yang (2008), SHRIMP U-Pb zircon geochronology of Neoproterozoic Korla mafic dykes in the northern Tarim Block, NW China: Implications for the long-lasting breakup process of Rodinia, *J. Geol. Soc. London*, *165*, 887–890, doi:10.1144/0016-76492007-174.
Zhu, W. B., B. H. Zheng, L. S. Shu, D. S. Ma, H. L. Wu, Y. X. Li, W. T. Huang, and J. J. Yu (2011a), Neoproterozoic tectonic evolution of the Precambrian Aksu blueschist terrane, northwestern Tarim, China: Insights from LA-ICP-MS zircon U-Pb ages and geochemical data, *Precambrian Res.*, *185*, 215–230, doi:10.1016/j.precamres.2011.01.012.
Zhu, W. B., B. H. Zheng, L. S. Shu, D. S. Ma, J. L. Wan, D. W. Zheng, Z. Y. Zhang, and X. Q. Zhu (2011b), Geochemistry and SHRIMP U-Pb zircon geochronology of the Korla mafic dykes: Constrains on the Neoproterozoic continental breakup in the Tarim Block, northwest China, *J. Asian Earth Sci.*, *42*, 791–804, doi:10.1016/j.jseaes.2010.11.018.
Zong, K. Q., Y. S. Liu, Z. M. Zhang, Z. Y. He, Z. C. Hu, J. L. Guo, and K. Chen (2013), The generation and evolution of Archean continental crust in the Dunhuang block, northeastern Tarim Craton, northwestern China, *Precambrian Res.*, *235*, 251–263, doi:10.1016/j.precamres.2013.07.002.